Forcing Function Estimation for Space System Rollout

George James[1], Robert Grady[1], Matt Allen[2], and Erica Bruno[3]

[1]Structural Engineering Division,
NASA Johnson Space Center, Houston, TX 77058

[2] Engineering Physics Department
University of Wisconsin-Madison, Madison WI 53706

[3]Analytical Mechanics Associates, Hampton, VA 23666

ABSTRACT
American crewed spaceflight systems have used a significant tracked transportation system to rollout the stacked vehicle and launch platform from the Vehicle Assembly Building (VAB) to the launch pad. This system has been shown to produce specific narrow-band harmonic forces that can excite the complete system, including the ability to force a resonance for long periods of time. This work reports on the efforts to develop tools and processes to reconstruct rollout forcing functions to support advanced needs for the extraction of dynamic properties. The multi-step processes provided in this work include a hybrid version of a traditional force reconstruction approach; transfer of expected CG forces to the assumed force input locations; expansion of the forces to a full-rank set of input forces; application of known dynamic constraints; and joint updating of FRFs and the estimated forces.

Three levels of success criteria are suggested for these processes as applied to analytical, laboratory, or measured field data: synthesizing output accelerometer data; reconstructing input forcing functions; and estimating modal properties. A dynamically simple system, limited instrumentation, and a simple single-speed forcing function are used to provide measured and analytical data to exercise and assess the tools of interest. Useful comparisons supporting the first success criteria are provided. Data and insight are also provided for the second success criteria. The simplicity of the example system supporting the work reported in this paper does not yet support the development of significant insight on the third success criteria. Follow-on activities are recommended to add additional insight into the process success with all three criteria.

This work not only addresses engineering development work of specific and unique interest to spaceflight systems but also suggests general applicability for force estimation, dynamic property estimation, and operational testing situations. Specifically these tools are to enable the estimation of dynamic properties when the loading and constraint environments complicate traditional OMA techniques. Unique contributions of this process include: expanding inputs and constraints of traditional force reconstruction techniques; using null space vectors to complete the basis set for full rank force reconstruction; and constraining linear solutions to filter estimated forces for targeted force updating.

Keywords: Operational Testing, Force Reconstruction, Experimental Modal Analysis, Operational Modal Analysis, Harmonic Loading

INTRODUCTION

The current era of manned spaceflight development targets increasing efficiency in the use of test articles and flight hardware to maximize data return. When structural dynamic information is of interest, Operational Modal Analysis (OMA) techniques can be used to extract parameters from a wide variety of field, operations, and secondary situations [1-6]. However, OMA techniques can become difficult to use when the forcing functions become complicated [7] or the system changes rapidly [8]. One goal of this work is to identify the forcing function from OMA measurements, and then to use it as an input to standard input-output tools from experimental modal analysis (EMA), for example when estimating frequency-response functions. The targeted operational scenario used in this paper is that of the rollout loading as a space system is transported to the launch

pad. Many NASA manned vehicles have made the final transportation to the launch pad via a significant track/tread based system called the Crawler-Transporter (CT) coupled to a mobile version of the launch pad. Figure 1 depicts the Space Transportation System (STS) vehicle (Space Shuttle) and the associated Mobile Launch Platform (MLP) under transport to the launch site using this system.

Besides the STS, the same CT system has been used to move multiple versions of the Apollo/Saturn vehicles, multiple test versions of the STS hardware, the Ares1-X vehicle, the Mobile Launcher (ML) for the now-cancelled Constellation systems, and the ML for the future Space Launch System (SLS) [9]. Based on this experience, this "Rollout" event has been found to have the potential to produce structural and fatigue loads on large flexible launch vehicles and spacecraft. On the other hand, this experience has shown that there is a potential to use the resultant rollout loading to exercise the vehicle for structural dynamic properties of the vehicle and launch platform [7, 9-12]. Dedicated tests have been used to exercise and develop this operational environment for use as supplemental modal tests.

In previous STS-era work on the rollout forcing functions, the primary effort was to estimate the forcing functions at measured and interpolated speeds to identify speed ranges that caused undesired loading events [3, 7, 10]. The historical work is a useful basis for initiating the current effort but was not driven by the same high-fidelity need to exercise the forcing functions as the current work. Previously, the forcing functions were estimated using a modification of the Sandia National Laboratories-developed Sum of Weighted Accelerations Technique (SWAT) [13, 14]. The modifications to SWAT resulted in a hybrid approach that used the mode shapes of the structural model to estimate weighting matrices used to convert measured accelerations into estimated forces. Estimated six Degrees-Of-Freedom (DOF) forces then drove a free-free model (to meet the requirements of the traditional SWAT process [13]) of the STS vehicle and Mobile Launch Platform (MLP) at the center-of-mass. The resulting functions were then scaled to generate roll-out forcing functions at speeds between the measured data. This process allowed the dynamic model of the structure to be used to estimate the response at a wider range of speeds. The problems with this approach are the reliance on a CG input point, a limited frequency range constrained by the number of measurement locations, and the reliance on the analytical Finite Element Model (FEM) of the vehicle.

Work with the Ares I-X vehicle, the cancelled Constellation Program systems, and the in-development SLS have highlighted potential uses of the expanded STS-era data to estimate rollout forcing functions, develop fatigue spectra, perform operational diagnostics, and extract structural dynamic properties. As a result, NASA has worked to overcome two STS-era shortcomings listed above (center-of-mass input and limited frequency range) and directly feed the processes reported in this work [15, 16]. The work reported in this paper includes the previous advances but also jointly estimates forcing functions and transfer functions without reliance on the dynamic FEM.

Figure 1: Space Shuttle Launch Vehicle Undergoing Rollout to the Pad for Launch

DATA PROCESSING STEPS

Overview of Data Processing Steps

A set of 14 data processing steps (some of which are optional) have been set up and coded to process the rollout data. A historical .9mph rollout data set has been used to exercise and assess the process. The process description, numerical examples, and experimental results were exercised using 63 measured accelerations from the CT+MLP system (as described in Appendix A) to estimate 12 input forces at locations on the CT trucks below the JEL system. The final products are estimated forcing functions, Frequency Response Functions (FRFs), and Impulse Response Functions (IRFs) that can be processed to extract modal parameters with little or no forcing function harmonics represented in the modal estimates. A summarized list of the processing steps follows:

- *Step #0 - Set Input Parameters and Filter Data*
  - The original time history data is subjected to numerical transforms and filters to allow comparisons with reconstructed data;
- *Step #1 – Calculate Rigid Body Modes*
  - Sensor geometry is used to estimate six rigid body modes in support of force reconstruction;
- *Step #2 – Remove Rigid Body Contribution from Original Data*
  - Removing rigid body contributions from the measured data provides the residual flex-body data
- *Step #3 – Determine Basis Vectors for Residual Flex-Body Data*
  - Left singular vectors become basis vectors for use in Step #4;
- *Step #4 – Determine SWAT Weight Matrix and CG Acceleration*
  - Standard SWAT processing is used once the basis is known to enable Step #5 by providing the weight matrix and CG accelerations;
- *Step #5 – Define CG Forces, Below-JEL Transformation, and Below-JEL Forces*
  - Forces and moments at the Center of Gravity (CG) are estimated and transferred to the input locations;
- *Step #6 – Define Below-JEL Null Space Transformation Vectors for Below-JEL Flex Forces*
  - Transformation matrix null space vectors are estimated (for use as basis vectors to complete the input forces in Step #8 or Step #9);
- *Step #7 – Scale 12 Below-JEL Accelerations with Assumed Mass at Each Corner*
  - Measured driving point accelerations are mass-scaled to provide an initial estimate of the Below-JEL forces (subject to modification in subsequent steps);
- *Step #8 – Estimate Total Below-JEL Forces*
  - Initial force estimates from Step #7 (or updated force estimates of Step #11 or Step #12) are filtered to enforce known constraints;
- *Step #9 – Alternative Estimation of Total Below-JEL Forces*
  - Alternate approach to Step #8 resulting in filtered force estimates with additional constraints;
- *Step #10 – Determine FRF between Total Below-JEL Forces and Original Accelerometer Data*
  - Calculate a transfer function and inverse transfer function between estimated forces and measured outputs;
- *Step #11 – Iterate Using Inverse FRF*
  - Use the measured outputs and estimated inverse transfer function to iteratively update the force estimates;
- *Step #12 – Iterate Using Assumed Residual Basis*
  - Alternative iteration force updating using Step #8 or Step #9 force filtering; and
- *Step #13 – Final Averaged FRF*
  - Create a final transfer function for modal processing from final forces and measured outputs.

Step #0 - Set Input Parameters and Filter Data

Step #0 conducts initial filtering and sliding window processing of the measured acceleration data. Subsequent processes will utilize specific estimation and synthesis of acceleration time histories from weighted averages of windowed data segments generated from frequency domain processes using the same sliding window transform. Therefore, Step #0 subjects the original measured data to similar filter, segment, transform, weight, and average processing to allow direct comparisons

to later synthesized data. A critical input parameter s defined in Step #0 (and used in subsequent steps) is the data segment window size that is used (denoted as *winsize*). Additionally, there are two overlap or window increment parameters. The first increment (denoted as *winskip0*) defines the number of overlaps and the size of the increment from one window to the next to be used in frequency domain estimations of Frequency Response Function (FRF) transfer function spectra. The second incrementing parameter used (denoted as *winskip1*) is the increment used when reconstructing a time history from frequency domain estimates of the response of *winsize* lengths. The low-pass frequency cut-off is defined and applied to the measured data in this step as well.

For the sliding window processing, a segment of *winsize* samples is extracted from the original data starting with time step 1 and incremented by *winskip1* samples for subsequent segments. The data segment is converted to the frequency domain via a Fast Fourier Transform (FFT). Note that if the full length of the time history is not used in the defined segments, an additional segment ending with the last data point (and the necessary beginning point) will be used to assure that the total length of the filtered time history is unchanged. The frequency filtered response is then converted back to the time domain with a symmetric inverse Fourier transform. The resulting *winsize* time segment is scaled by the *weight* vector (defined below) and added to a data collector vector (maintaining the original segment times). The data collector is a running, weighted sum of the estimates of the filtered accelerations at each time step and is represented in Equation (1):

$$X_C(t_j\colon t_j+\Delta t) = X_C(t_j\colon t_j+\Delta t) + weight.* X_j^o \; ; \tag{1}$$

where, $X_C(t_j\colon t_j+\Delta t)$ is the slice of the acceleration time history collector associated with the j^{th} increment;
X_j^o is the original acceleration time history computed for the j^{th} increment;
j is the increment number;
t_j is the time step at which the j^{th} increment starts;
Δt is the time increment or *winsize* sample increments;
weight is the numerical weighting vector;
".*" is a numerical operation that multiplies each entry in the two vectors; and
":" is a function symbol for a sweep over the number of time steps in a time increment.

The numerical weighting vector (denoted as *weight*), is composed of all integers starting with 1 and building sequentially to *winsize*/2 in the first half of *weight*. The values then reduce sequentially from *winsize*/2 to 1 for the last half of *weight*. The *weight* vector is to force time domain averages to place more emphasis on time points near the middle of a data window and de-emphasize the endpoints. An associated numerical collector, of the same length as each time history, is also updated by adding the weight vector to the same segment times. This numerical counter tracks how many weighted estimates have been added to the collector at each time step:

$$num_C(t_j\colon t_j+\Delta t) = num_C(t_j\colon t_j+\Delta t) + weight\,. \tag{2}$$

The process is repeated by shifting the original time increment window forward in time by the chosen number of samples (*winskip1*). The ideal shift is one time sample per increment, which creates a slow process but eliminates periodic data spikes resulting in numerical frequency content due to the periodic window shifts. However, the weighting of the data and numerical counter reduce these data spikes by adding weight to the filtered data at the center of each segment. At the end of the process, the data collector value at each time step is divided by the counter value at each time step to weight average the collector estimates at each time step and generate the final updated force time history (*X*):

$$X(t_j) = \frac{X_C(t_j)}{num_C(t_j)}\,. \tag{3}$$

Each original sensor time history is processed in this manner. It should be noted that a similar non-weighted version of this collector/averaging approach was used in Reference (15). The filtered version of the original data enables the use of relevant convergence metrics and comparison plots in subsequent processing steps. It should be noted that, this sliding window

processing has been shown to have minimal effect on the original measured data, which provides confidence that the technique will not add unwanted bias errors to subsequent processing steps.

Step #1 – Calculate Rigid Body Modes

Step #1 uses the sensor geometry to estimate the six rigid body modes (denoted by φ_{rb}) with respect to the Center of Gravity (CG) using the procedures provided in Reference (14). Note that the size of φ_{rb} is n_{res} *x 6*, where n_{res} is the number of measured acceleration sensors.

The following description will be limited to the case of each sensor output defined as a single orthogonal rectangular coordinate direction aligned with the system coordinate system. For this work, the translational rigid body shapes are denoted as the first 3 columns of φ_{rb} (X direction = 1, Y direction = 2, and Z direction = 3) and are defined as follows:

$$\varphi_{rb}(i,j) = \delta_{jk}; \tag{4}$$

where *i* denotes the sensor #,
j denotes the rigid body shape translational direction (1, 2, or 3),
k denotes the sensor direction (1, 2, or 3), and
$\delta_{jk}$is the delta function which is only a non-zero value (1.0) if *j* = *k* (1, 2, or 3).

For the rotation about the *X*, *Y*, or *Z* direction rigid body shapes (columns 4, 5, and 6 of φ_{rb}):

$$\varphi_{rb}(i,j) = \left[\begin{Bmatrix}1\\0\\0\end{Bmatrix} \times \begin{Bmatrix}L_X\delta_{lk} - CG_X\\L_Y\delta_{lk} - CG_Y\\L_Z\delta_{lk} - CG_Z\end{Bmatrix} \quad \begin{Bmatrix}0\\1\\0\end{Bmatrix} \times \begin{Bmatrix}L_X\delta_{lk} - CG_X\\L_Y\delta_{lk} - CG_Y\\L_Z\delta_{lk} - CG_Z\end{Bmatrix} \quad \begin{Bmatrix}0\\0\\1\end{Bmatrix} \times \begin{Bmatrix}L_X\delta_{lk} - CG_X\\L_Y\delta_{lk} - CG_Y\\L_Z\delta_{lk} - CG_Z\end{Bmatrix}\right]; \tag{5}$$

where, *i* denotes the sensor #,
j denotes the rigid body shape rotational direction (4, 5, or 6),
k denotes the sensor direction (*1 = X, 2=Y, or 3=Z*),
l denotes the relevant sensor coordinate (*l = j – 3* and *1 = X, 2=Y, or 3=Z*),
$\delta_{lk}$is the delta function which is only a non-zero value (1.0) if *l* = *k* (1, 2, or 3),
CG_k is the CG location in the k^{th} direction, and
L_k is the geometric coordinate of sensor #*i* in the k^{th} direction.

Step #2 – Remove Rigid Body Contribution from Original Data

This step involves performing a least squares fit of the rigid body modes to the original data and remove the resulting contribution to estimate the residual flexible body acceleration time histories. The following equation exemplifies this process:

$$\varphi_{rb} * X_{rb}(t) = X(t); \tag{6}$$

where X_{rb} are the *6 x n* rigid body amplitudes,
X are the n_{res} *x n* original measured accelerations, and
n is the number of measured time points.

The residual flexible body acceleration time histories (denoted by $X_1(t)$ of size n_{res} *x n*) are estimated as follows:

$$X_1(t) = X(t) - \varphi_{rb} * X_{rb}(t). \tag{7}$$

Step #3 – Determine Basis Vectors for Residual Flexible Body Data

The Singular Value Decomposition (SVD) is used in this step to determine a set of basis vectors for the flexible body residuals, which are needed to build a modified SWAT weight matrix (described in References [9, 10, 12-14]):

$$X_1 = U_1 * S_1 * V_1^T; \tag{8}$$

where U_1 is the n_{res} *x* n_{res} matrix of left singular vectors and the source of the desired basis vectors,
S_1 is the diagonal matrix of *nres* singular values; and
V_1 is the *n x nres* matrix of right singular vectors.

The flex body basis vectors (denoted by U_{r6} of size n_{res} *x* n_{r6} with $n_{r6} = n_{res} - 6$) are taken to be the n_{r6} left singular vectors associated with the largest n_{r6} singular values. The use of these basis vectors instead of mode shape vectors is the primary modification to a traditional SWAT approach.

Step #4 – Determine SWAT Weight Matrix and CG Acceleration
Step #4 uses the modified version of SWAT, which is a time-domain approach relating the forces at the CG to the accelerations at the CG. The initial step of SWAT involves developing a weight matrix (W of size *6 x* n_{res}), which allows the estimation of the CG accelerations (Note that this matrix is distinct from the w*insize* x 1 *weight* vector of Step #0):

$$X_{CG}(t) = W * X(t). \tag{9}$$

The weight matrix is chosen to sum the measured accelerations to generate estimates for each of the six rigid body accelerations at the CG. In performing this estimation, the chosen elastic body generalized DOFs and all rigid body generalized modes (except the single rigid body mode of interest) are zeroed out. The rigid body modes and flexible basis vectors are collected into a matrix φ_T of size n_{res} *x* n_{res} (with the first six vectors providing the rigid body modes), which will be used to build the weight matrix:

$$\varphi_T = [\varphi_{rb}, U_{r6}]. \tag{10}$$

The weight matrix is estimated (which nulls the elastic mode shapes and unit normalizes the rigid body shapes) as depicted in equations (6) and (7):

$$W_i * \varphi_{T_k} = \delta_{ik}; \tag{11}$$

with i and k sweeping the columns of W and φ; and
δ_{ik} is the delta function which is only a non-zero value (1.0) if $i = k$ (the first 6 vectors).

Step #5 – Define CG Forces, Below-JEL Transformation, and Below-JEL Forces
The forces at the CG (denoted by F_{CG} of size *6 x n*) are related to the accelerations at the CG via the *6 x 6* global mass matrix defined at the CG (denoted as M_{CG}):

$$F_{CG}(t) = M_{CG} X_{CG}(t). \tag{12}$$

The global mass matrix is defined about the CG as follows:

$$M_{CG} = \begin{bmatrix} M_T & 0 & 0 & & & \\ 0 & M_T & 0 & & 0 & \\ 0 & 0 & M_T & & & \\ & & & I_{XX} & I_{YX} & I_{ZX} \\ & 0 & & I_{XY} & I_{YY} & I_{ZY} \\ & & & I_{XZ} & I_{YZ} & I_{ZZ} \end{bmatrix}; \tag{13}$$

where M_T is the total mass of the system; and
I_{XX}, I_{YY}, I_{ZZ}, I_{XY}, I_{XZ}, I_{YZ}, I_{ZX}, I_{ZY}, and I_{YX} are the Moments Of Inertia (MOI) and Products Of Inertia (POI).

Step #5 then uses the 3x3 Below-JEL force to CG moment transformation cross product matrices to convert forces at the CG to forces at the desired below-JEL locations, which are defined as:

$$\chi_i = \left[\begin{Bmatrix} L_X - CG_X \\ L_Y - CG_Y \\ L_Z - CG_Z \end{Bmatrix} \times \begin{Bmatrix} 1 \\ 0 \\ 0 \end{Bmatrix} \quad \begin{Bmatrix} L_X - CG_X \\ L_Y - CG_Y \\ L_Z - CG_Z \end{Bmatrix} \times \begin{Bmatrix} 0 \\ 1 \\ 0 \end{Bmatrix} \quad \begin{Bmatrix} L_X - CG_X \\ L_Y - CG_Y \\ L_Z - CG_Z \end{Bmatrix} \times \begin{Bmatrix} 0 \\ 0 \\ 1 \end{Bmatrix}\right] = [R_i \times \hat{e}_X \quad R_i \times \hat{e}_Y \quad R_i \times \hat{e}_Z]; \tag{14}$$

where, CG_j is the CG location in the j^{th} direction;
L_j is the location of the i^{th} Below-JEL force input location in the j^{th} direction;
R_i is the vector from the CG to the i^{th} Below-JEL force input location; and
$\hat{e}$ are the basis unit vectors of each axis.

Hence the *6 x 12* transformation matrix (T_χ and after normalization T) can be generated to convert the 6 DOF forces at the CG (F_{CG}) to the 12 DOF forces defined Below-JEL (F_{bj} of size *12 x n*):

$$F_{CG_\chi} = \begin{bmatrix} F_F \\ F_{R_\chi} \end{bmatrix} = \begin{bmatrix} I & I & I & I \\ \chi_A & \chi_B & \chi_C & \chi_D \end{bmatrix} \begin{bmatrix} F_A \\ F_B \\ F_C \\ F_D \end{bmatrix} = T_\chi * F_{bj}; \tag{15}$$

where, F_A, F_B, F_C, and F_D are the *3 x n* Below-JEL estimated translational forces at each truck;
χ_A, χ_B, χ_C, and χ_D are the Below-JEL force to CG moment transformation cross products; and
I is the *3 x 3* identity matrix.

It makes numerical sense to normalize F_R to balance the T_χ matrix:

$$\chi_N = \sqrt[2]{({\chi_A}^2 + {\chi_B}^2 + {\chi_C}^2 + {\chi_D}^2)}; \text{ and} \tag{16}$$

$$F_{CG} = \begin{bmatrix} F_F \\ F_R \end{bmatrix} = \begin{bmatrix} F_F \\ \frac{F_{R_\chi}}{\chi_N} \end{bmatrix} = \begin{bmatrix} I & I & I & I \\ \frac{\chi_A}{\chi_N} & \frac{\chi_B}{\chi_N} & \frac{\chi_C}{\chi_N} & \frac{\chi_D}{\chi_N} \end{bmatrix} \begin{bmatrix} F_A \\ F_B \\ F_C \\ F_D \end{bmatrix} = T * F_{bj}; \tag{17}$$

Note that the order of the entries in the F_{bj} vector are as follows:

$$F_{bj} = \begin{bmatrix} F_{bj_{AX}}(t_0) & \cdots & F_{bj_{AX}}(t_n) \\ \vdots & \ddots & \vdots \\ F_{bj_{DZ}}(t_0) & \ldots & F_{bj_{DZ}}(t_n) \end{bmatrix}; \tag{18}$$

where A, B, C, and D denote the corner; and
X, Y, and Z denote direction of force.

And the order of entries in the F_{CG} matrix is as follows:

$$F_{CG} = \begin{bmatrix} F_F \\ F_R \end{bmatrix} = \begin{bmatrix} F_{F_X}(t_0) & \cdots & F_{F_X}(t_n) \\ F_{F_Y}(t_0) & \ldots & F_{F_Y}(t_n) \\ F_{F_Z}(t_0) & \ldots & F_{F_Z}(t_n) \\ F_{R_X}(t_0) & \cdots & F_{R_X}(t_n) \\ F_{R_Y}(t_0) & \ldots & F_{R_Y}(t_n) \\ F_{R_Z}(t_0) & \ldots & F_{R_Z}(t_n) \end{bmatrix}; \tag{19}$$

where F_F denotes translational force at the CG, and
F_R denotes rotational moment at the CG.

At this point, the Below-JEL forces are a rank deficient partition that drives the CG accelerations via rigid body modes. Hence in order to solve Equation (17) for F_{bj}, an SVD pseudo-inversion is used. The resulting answer will be of rank 6. However, a full rank rigid body plus flex body solution will result from later steps.

Another solution approach is to assume that F_{bj} is defined to be a linear combination of the basis vectors (*12 x 6* left singular vectors of T^T denoted as *U*), which can be defined with a Singular Value Decomposition (SVD):

$$U * S * V^T = T^T. \tag{20}$$

$$F_{bj} = U * \alpha; \tag{21}$$

where α is the *6 x n* matrix of scale factors for the basis vectors of *T* to create F_{bj}.

Note that system-level mass properties [MOI, POI, and CG location,] as well as sensor geometry are known and represent the only parameters that are extracted from an FEM.

Step #6 – Define Below-JEL Null Space Transformation Vectors for Below-JEL Flex Forces

The Below-JEL forces (F_{bj}) developed in the previous step are necessarily a rank deficient partition that drives the CG accelerations via rigid body modes. Hence the approach implemented in this step estimates the non-rigid body partition of the Below-JEL forces (F_{f6}) to complete the rank and drive the flex-body part of the measured accelerations:

$$F_T = F_{bj} + F_{f6}. \tag{22}$$

The assumption is that F_{f6} will be defined as a linear combination of the six vectors (denoted by *N* of size *12 x 6*) that span the null space of the transformation matrix *T*:

$$N = null(T). \tag{23}$$

$$F_{f6} = N * \beta; \tag{24}$$

where β is the *6 x n* matrix of scale factors for the null space of *T* vectors to create F_{f6}.

Note that assessing the Step #6 process is one of the key contributions of this work, since this is a unique enhancement over previous work in these applications.

Step #7 – Scale 12 Below-JEL Accelerations with Assumed Mass at Each Corner

Step #7 captures the fact that the CT system carries a different amount of the total weight at each corner truck. The weight ratios for each corner can be measured (using the CT JEL system pressures) or estimated from the mass properties of the system. Denote the scale factor for each corner as $\propto_A$, $\propto_B$, $\propto_C$, and $\propto_D$. Hence the mass at each corner is defined as:

$$M_A = \propto_A * M_T. \tag{25}$$

$$M_B = \propto_B * M_T. \tag{26}$$

$$M_C = \propto_C * M_T. \tag{27}$$

$$M_D = \propto_D * M_T \tag{28}$$

Now it will become useful to scale the 12 measured Below-JEL measured accelerations by the mass carried at each corner to convert to force units:

$$F_M = \begin{bmatrix} M_A * X_{bj_{AX}}(t_0) & \cdots & M_A * X_{bj_{AX}}(t_n) \\ \vdots & \ddots & \vdots \\ M_D * X_{bj_{DZ}}(t_0) & \cdots & M_D * X_{bj_{DZ}}(t_n) \end{bmatrix} = M_{bj} * X_{bj}. \tag{29}$$

In subsequent steps, F_M takes on the roles of an initial starting estimate of a FF as well as a numerical tool to relate Below-JEL forces to Below-JEL accelerations. It should be noted that the definition of higher-fidelity starting estimates is an active area of development for this work.

Step #8 – Estimate Total Below-JEL Forces

Step #8 and Step #9 are alternative approaches to refine the current estimates of the forcing function (including the Step #7 initial estimate). It should be noted that Step #9 is an expansion of Step #8, so it is useful to review Step #8 first (although the Step #8 is not used in the data presented in this paper). Also it should be noted that assessing the Step #8/Step #9 processes are another major contribution of this work, since these steps are an expansion over previous work in these applications. For Step #8, F_M is related to F_T via a residual Below-JEL acceleration matrix, which allows Equation (22) to combine with Equation (29):

$$F_M - M_{bj}\Delta X_{bj} = F_T = F_{bj} + F_{f6} = U * \alpha + N * \beta. \tag{30}$$

And collecting Equation (30), Equation (21), and Equation (17):

$$\begin{bmatrix} F_T \\ F_{CG} \end{bmatrix} = \begin{bmatrix} U & N \\ T * U & 0 \end{bmatrix} * \begin{bmatrix} \alpha \\ \beta \end{bmatrix} = \begin{bmatrix} A_1 \\ A_2 \end{bmatrix} * [C] = \begin{bmatrix} B_1 \\ B_2 \end{bmatrix}. \tag{31}$$

For the initial iteration, it is assumed that $\Delta X_{bj} = [0]$. Hence using Equation (30), the initial F_T is equal to F_M. In later steps, Equation (31) will be solved with more refined estimates of the total Below-JEL force. Equation (31) can be solved by constrained least squares as provided in Reference [17]. The upper partition is the primary linear problem and the lower partition becomes constraint equations as follows:

$$C = \bar{C} + K(B_2 - A_2\bar{C}); \tag{32}$$

$$K = (A_1^t * A_1)^{-1}A_2^t(A_2(A_1^t * A_1)^{-1}A_2^t)^{-1}; and \tag{33}$$

$$\bar{C} = (A_1^t * A_1)^{-1}A_1^t B_1 \tag{34}$$

Note that it is assumed that U and N are normalized by definition, which makes A_1 an orthonormal matrix and simplifies Equations (32), (33), and (34). After solution, Equation (30) is used to generate the total force estimates at each time step since C is estimated at each time step. Although simpler solutions to Equation (31) are available, Step #9 is an alternative to Step #8 and builds on this structure.

Step #9 – Alternative Estimation of Total Below-JEL Forces

Step #9 provides an alternative and expanded approach to Step #8 (and the step actually used in the presented herein). It alternatively estimates the Below-JEL Forces by augmenting Equation (31) with equations to drive the output accelerations to match the complete set of measured responses across the vehicle. This process can be enabled using the left singular vectors (U_1) for the flexible-body part of the accelerations as in Equation (8) or using the left singular vectors of the total measured acceleration matrix:

$$X = U_1 * S_1 * V_1^T; \tag{35}$$

Note that the matrix designation of U_1 is used in both equation (8) and equation (35), since X and X_1 are largely interchangeable in Step #9. The remainder of this discussion will assume that X is used as opposed to X_1. It can therefore be assumed that the X matrix can be reconstructed with a linear combination of the left singular vectors scaled at each time step:

$$X = U_1 * \gamma = \begin{bmatrix} U_{1_U} \\ U_{1_L} \end{bmatrix} * \gamma = \begin{bmatrix} X_U \\ X_L \end{bmatrix} = \begin{bmatrix} X_{bj} \\ X_L \end{bmatrix}; \tag{36}$$

where the "U" denotes the first 12 entries which are assumed to be the Below-JEL measurements; and
the "L" designator denotes the remaining $n_{res} - 12 = n_{r12}$ sensors.

The full fit from Equation (36) is used to augment the A_1 and B_1 matrices of Equation (31):

$$\begin{bmatrix} F_T \\ X \end{bmatrix} = \begin{bmatrix} U & N & 0 \\ 0 & 0 & U_1 \end{bmatrix} * \begin{bmatrix} \alpha \\ \beta \\ \gamma \end{bmatrix} = B_1 = A_1 C. \tag{37}$$

As with Equation (31), matrix A_1 is orthonormal here as well and the transpose equals the inverse.

The upper partition of Equation (36) is combined with Equation (30) to become an augmented constraint equation.

$$\begin{bmatrix} F_{CG} \\ F_T - F_M \end{bmatrix} = \begin{bmatrix} T * U & 0 & 0 \\ U & N & -M_{bj} * U_{1_U} \end{bmatrix} * \begin{bmatrix} \alpha \\ \beta \\ \gamma \end{bmatrix} = B_2 = A_2 C. \tag{38}$$

The constraint equations are used to assure that the rigid body part of the FF maintains the expected force at the CG as well as to assure that the flex body and rigid body part of the Below-JEL accelerations match up with the below JEL accelerations. Equations (32), (33), and (34) are again used to solve these equation and the updated total force is reconstructed using Equation (30). Equation (38) can be used with an initial guess of $F_T = F_M$ or can be used to modify an updated F_T to assure that the constraints are met during iterative processing.

Step #10 – Determine FRF between Total Below-JEL Forces and Original Data

Estimate FRF

Step #10 takes the current force estimates and the measured responses to estimate a Frequency Response Function (FRF). The Total Least Squares using an SVD approach as discussed in Reference [18] is the primary approach for FRF estimation (denoted as H_4) used in this work. However, other common approaches as implemented in Reference [15] can be used (denoted as H_1, H_2, and H_3).

Under the H_4 approach, the frequency domain version of the input and output for each *winsize/winskip0* segment are collected (each row is a different segment and each column is a different force or measured acceleration) into the same matrix representation (Y):

$$[Y(\omega)]^H = [[F_T(\omega)]^H \quad [X(\omega)]^H] = [U_Y][S_Y][V_Y]^H; \tag{39}$$

Where U_Y is the matrix of left singular vectors of Y;
S_Y is the diagonal matrix of non-zero singular values of Y; and
V_Y is the matrix of right singular vectors of Y.

Therefore, the total least squares FRF is given by the following:

$$[H_4] = [V_{YX12}][V_{YF12}]^{-1}. \tag{40}$$

where:

$$[V_Y] = \left[[V_{Y12}][V_{Yn12}]\right] = \begin{bmatrix} [V_{YF12}] & [V_{YFn12}] \\ [V_{YX12}] & [V_{YXn12}] \end{bmatrix}. \tag{41}$$

The subscripts defining the partitions of V_Y in Equation (41) can be interpreted as follows: (1) $_{F12}$ are first *nref* columns and *nref* rows; (2) $_{X12}$ are the first *nref* columns and last nres rows; (3) $_{Fn12}$ are the last *nres* columns and the first *nref* rows; and (4) $_{Xn12}$ are the last *nres* columns and the last *nres* rows. The "*nref*" descriptor refers to the number of assumed references or inputs (12 in the case of the data provided in this paper). The "*nres*" descriptor refers to the number of measured responses or outputs (63 in the case of the data provided in this paper).

Estimate Inverse FRF

Step #10 also estimates an inverse transfer function called G_4 by performing a pseudoinverse of H_4:

$$[G_4] = [V_{YFnres}][V_{YXnres}]^{-1}. \tag{42}$$

Where:

$$[V_Y] = \left[[V_{Ynres}][V_{Y12}]\right] = \begin{bmatrix}[V_{YXnres}] & [V_{YX12}] \\ [V_{YFnres}] & [V_{YF12}]\end{bmatrix}. \tag{43}$$

Previous work on these systems directly applied Equations (39), (40), and (41) with the role of accelerations and forces reversed, but that option has not been exercised in this work reported in this paper [9].

Estimate Delta X

For the full size FRF approach, the estimated forces and FRF can be used to reconstruct the measured sensors (X) and the resulting residuals (Δ_X):

$$[H_4(\omega)][F(\omega)] = [X_s(\omega)] = [X(\omega)] + [\Delta_X(\omega)]. \tag{44}$$

The full time history of the synthesized accelerations would use the process covered in Equations (1), (2), and (3). Subsequent iterations would attempt to drive the residual from Equation (44) towards zero and therefore reproduce the measured accelerations.

Estimate Delta F

The inverse FRF approach can be used to estimate updates to the 12 DOF forcing functions using the 1st order assumed FRF process (for the i^{th} iteration):

$$[F_{i+1}(\omega)] = [H_4(\omega)]^{-1}[X(\omega)] = [G_4(\omega)][X(\omega)] = [F_i(\omega)] + [\Delta_{Fi}(\omega)]. \tag{45}$$

In a similar fashion, the full time history of the updated Below-JEL forces use the same collector/averaging process as was used for the Step #0 acceleration measurement filtering and the Step #10 acceleration synthesis. After conversion of each increment to the time domain, the *winsize* length time records are weighted and added to a collector vector for each time record. The collector is a running weighted sum of the estimates of the updated forces at each time step (denoted as j):

$$F_C(t_j\colon t_j + \Delta t) \;= F_C(t_j\colon t_j + \Delta t) + weight * F_j\;; \tag{46}$$

where, $F_C(t_j\colon t_j + \Delta t)$ is the slice of the force time history collector associated with the j^{th} increment;
F_j is the force time history computed for the j^{th} increment;
j is the increment number;
t_j is the time step associated with the j^{th} increment;
Δt is the time increment; and
: is a function symbol for a sweep over the number of time steps in a time increment.

A numerical counter of the same length as each time history is updated when each time increment is added to the collector to track how many weighted estimates have been added to the collector at each time step:

$$num_C(t_j\colon t_j + \Delta t) \;= num_C(t_j\colon t_j + \Delta t) + weight\,. \tag{47}$$

The process is repeated by shifting the original time increment window forward in time by the chosen number of samples. The ideal shift is one time sample per increment, which creates a slow process but eliminates periodic data spikes resulting in numerical frequency content due to the periodic window shifts. However, the weighting process reduces the data spikes by giving more weight to the estimates in the middle of each segment. At the end of the process, the collector value at each time step is divided by the weighted numerical counter value at that time step to average the weighted estimates and generate an updated force time history:

$$F_{i+1}(t) = \frac{F_C}{num_C}\,. \tag{48}$$

Convergence Metrics

Since Step #10 may be performed multiple times to support either Step #11 or Step #12 iterations, therefore eight metrics have been identified to monitor the changes that result. The eight metrics include the following (where *norm* is the 2-norm of a matrix, *max* picks the maximum value, and *abs* calculates the absolute value):

$$X_{norm} = \frac{norm(X+\Delta X_{i+1})}{norm(X)} - 1.0; \tag{49}$$

$$X_{max} = \frac{max(abs(X+\Delta X_{i+1}))}{max(abs(X))} - 1.0; \tag{50}$$

$$F_{norm} = \frac{norm(F_{i+1})}{norm(F_i)} - 1.0; \tag{51}$$

$$F_{max} = \frac{max(abs(F_{i+1}))}{max(abs(F_i))} - 1.0. \tag{52}$$

$$H_{norm} = \frac{norm(H_{4_{i+1}})}{norm(H_{4_i})} - 1.0; \tag{53}$$

$$H_{max} = \frac{max\left(abs(H_{4_{i+1}})\right)}{max\left(abs(H_{4_i})\right)} - 1.0; \tag{54}$$

$$G_{norm} = \frac{norm(G_{4_{i+1}})}{norm(G_{4_i})} - 1.0; and \tag{55}$$

$$G_{max} = \frac{max\left(abs(G_{4_{i+1}})\right)}{max\left(abs(G_{4_i})\right)} - 1.0. \tag{56}$$

Step #11 – Iterate Using Inverse FRF

Step #11 represents a simplistic approach to updating the forcing function estimates. It should be noted that Step #12 is used in the examples provided in this paper. However, it is instructive to review Step #11 before reviewing the more complex Step #12 (as with Step #8 and Step #9 previously). Step #11 (or Step #12) is initiated with one of three approaches (note option #3 coupled with Step #12 will be used in the examples reported herein):

1. Perform an initial Step #10 calculation process (with $F_T = F_M$) and iterate using the results of Equation (45) to Equation (48);
2. Update F_M with the Step #8 process to enforce the F_{CG} forces, perform a Step #10 calculation process, and iterate using the results of Equation (45) to Equation (48); or
3. Update F_M with the Step #9 process to enforce the F_{CG} forces and enforce the link to vehicle acceleration, perform a Step #10 calculation process, and iterate using the results of Equation (45) to Equation (48);.

Step #11 would continue using a second (and as needed subsequent) Step #10 update to the FRF Transfer Function feeding the subsequent reapplication of Equation (57):

$$[Y_{i+1}]^H = [[F_{i+1}]^H \quad [X]^H]. \tag{57}$$

The process would iterate until convergence with no additional per-iteration modification of the estimated forces from the Step #8 or Step #9 processes. Iterations end when either one of four metrics defined above (X_{norm}, X_{max}, F_{norm}, *or* F_{max}) fall below a pre-defined threshold or when a maximum number of iterations are reached. Note that most exercises performed to-date terminate with the maximum number of iterations not via a convergence metric.

Step #12 – Iterate Using Assumed Residual Basis

Step #12 is initiated with one of the three iteration options listed above in Step #11. Unlike Step #11, Step #12 modifies the current FF estimates using either Step #8 or Step #9 to impose the implemented constraints. Hence, the major option choice for Step #12 is whether each iteration force update is filtered by a Step #8 or a Step #9 process before the reapplication of the

Step #10 calculation. Note that F_{i+1} is used to feed either Equation (31) or Equation (37) for each iteration. As noted previously, Step #9 and Step #12 are used in the examples reported in this work.

A second option includes a decision on keeping F_{CG} constant from iteration to iteration or updating F_{CG} each iteration using Equation (9) and Equation (12). The examples reported in this work do not update F_{CG}. F_{CG} is also an input to either Step #8 via Equation (31) or Step #9 via Equation (38). Iteration convergence metrics used to-date are the same as those provided in the equations (49) – (56). It should be noted that in the exercises performed to-date, little change in the convergence metrics are seen after the second iteration and the processing generally terminates after a defined number of iterations.

Step #13 – Final Averaged FRF

Once the final full length force time history is generated from the final iteration of Step #11 or Step #12, a final averaged FRF is generated per Step #10 with the final estimated force. This final FRF is intended to be used as-is for frequency domain modal parameter extraction. The FRF matrix is converted to the time domain using a symmetric Inverse Fourier Transform to generate Impulse Response Functions (IRFs) to allow time domain modal parameter extraction approaches to be exercised as well.

Initial Recommended Approach

Several processing options have been listed during the above description. Based on the experience to-date the following selections appear reasonable:

1. Step #9 is used as the initial force estimate option;
2. Full acceleration time histories (X) are used in Step #9 as opposed to flex-only accelerations (X_1);
3. Step #12 is used for iterations;
4. Step #9 is used for each iteration force filter;
5. F_{CG} is not updated each iteration;
6. Two forcing function iterations appear to be sufficient; and
7. A convergence threshold of 10^{-6} is used (but iteration limiting appears to be sufficient).

ANALYTICAL EXAMPLE

Success Criteria

Evaluation of the processes listed above is by three success criteria. The first required success criteria is the estimated FF and FRF will reproduce the measured acceleration data as subjected to the filters of Step #0. Note that this success criteria can be applied to either analytical or experimental data. The second success criteria will be based on the proper breakdown of the FF vs. the transfer function. This success criteria can only be applied to analytical data sets where the input forcing functions are known. The third success criteria are the applicability of the FRF/IRF for driving modal parameter estimation tools. The direct comparison to known modal frequencies and known mode shapes can only be exercised with analytical data sets with known properties. However subjective assessments of the applicability and ease of use of modal estimation tools can be made using experimental data sets.

Data Set and Processing Description

An analytical data set was developed using a free-free FEM of the CT+MLP system. Figure 2 provides the first 100 modes of this system (up to 100 Hz). Note that the first elastic modes are a pair at 4.37Hz. A FF previously estimated to represent this system operating at a speed of .9 mph for 10 minutes was simulated [15]. The 12 DOF inputs were applied at the Below-JEL locations denoted as sensors of 34, 35, 36, and 37 of Figure A4 and Table A1. Acceleration outputs at the locations described in Tables A1 and A2 were simulated. The process was then applied to estimate the forcing functions and the system FRFs and IRFs. For this exercise, the simulated output data was frequency filtered to 60Hz. A window size (*winsize*) of 16384 was used with a *winskip0* increment of 8192 samples for FRF calculations. The *winskip1* time domain averaging increment was 256 samples. When expanded views of the data are shown, the initial 1024 samples are used. Step #9 and Step #12 were used for two forcing function iterations. The F_{CG} forces were not allowed to update each iteration. Two iterations were allowed with forcing function updates and a final FRF calculation was made using the final forcing functions.

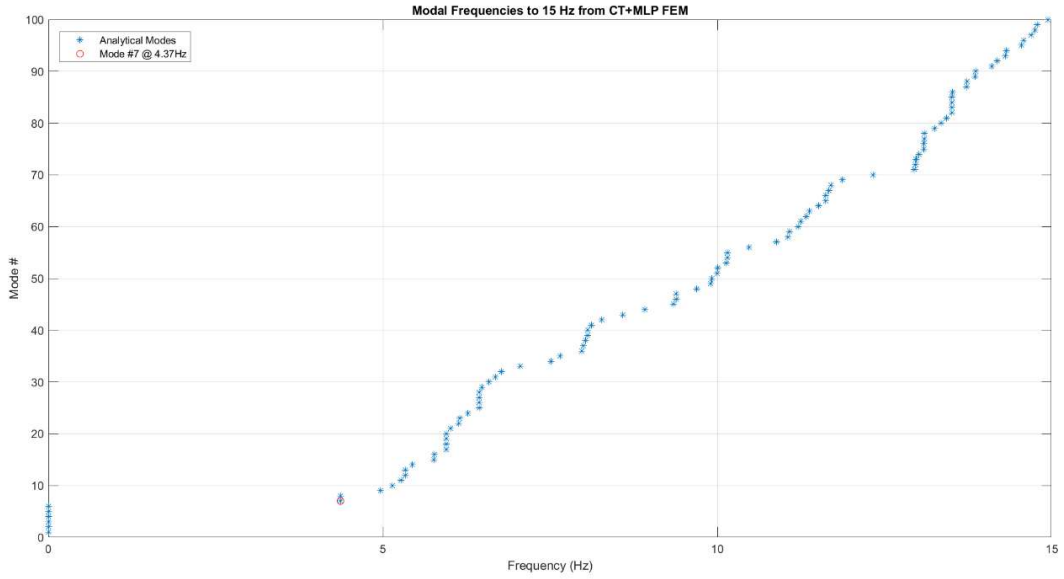

Figure 2: Modal Frequencies to 15 Hz from CT+MLP Finite Element Model (FEM)

Results and Discussion

An example of the data driving success criteria 1 is shown in Figure 3 which provides the simulated output at the driving point Below-JEL at Corner A in the vertical (X) direction. The upper part of the plot suggests that the general fit of the reconstructed to truth time signal is reasonable. The bottom plot shows that in the frequency domain some peaks were missed but the frequency content was captured fairly well overall. The middle plot shows an expanded time domain view of the first 1024 data points. This plot does show the effects of missing the amplitude of some of the higher amplitude peaks seen in the frequency domain. It should be noted that the first (and the last data points) of the reconstructed time history are the most challenging to fit due to the limited number of averages using the described approach. Figure 4 provides the same information for the lateral side-to-side (Y) direction above the JEL at the CT/MLP interface above Truck A. The fit up to 5 Hz is excellent but mismatch between truth and reconstruction sets in after 5 Hz. Figure 5 shows a fore/aft (Z) drive direction from the center of Side 3 of the upper MLP deck. This reconstruction is overall a better fit but does show some additional higher frequency mismatches. Overall, there is room for improvement in fitting the truth simulations.

Figures 6, 7, and 8 provide examples of data that drives the second success criteria. These plots show the reconstructed force inputs in the X, Y, and Z directions respectively at the Below-JEL location on Truck A as compared to the known original forces. In all cases the upper time domain plot shows that globally the comparisons are fairly reasonable but room for improvement is seen. The middle plots are again the challenging first 1024 points of each time history comparison. Here it can be seen the some of the higher amplitude peaks were not fit as well as could be but the frequency content is likely reasonable captured. The bottom plots illustrate overall the frequency content is captured well but the amplitudes are off in some frequency bands. In the X direction of Figure 6, the fit is very reasonable up to 5 Hz, but is significantly off between 5 and 10 Hz. In the Y direction of Figure 7, the fit to 6 Hz is excellent. However, above 6 Hz there is a consistent bias in the reconstruction of the forcing function. The Z direction of Figure 8 has frequency domain comparisons on the order of similar fits in the Y direction. Overall these reconstructed to original force comparisons are close enough to suggest that the procedures provided herein do hold promise for becoming a successful tool to support operational testing. One possible source of mismatch is the CT FEM which is not considered a correlated model. Additional sensors and speeds would improve the ability generate higher-fidelity force estimates by expanding the applicability of the SWAT forces.

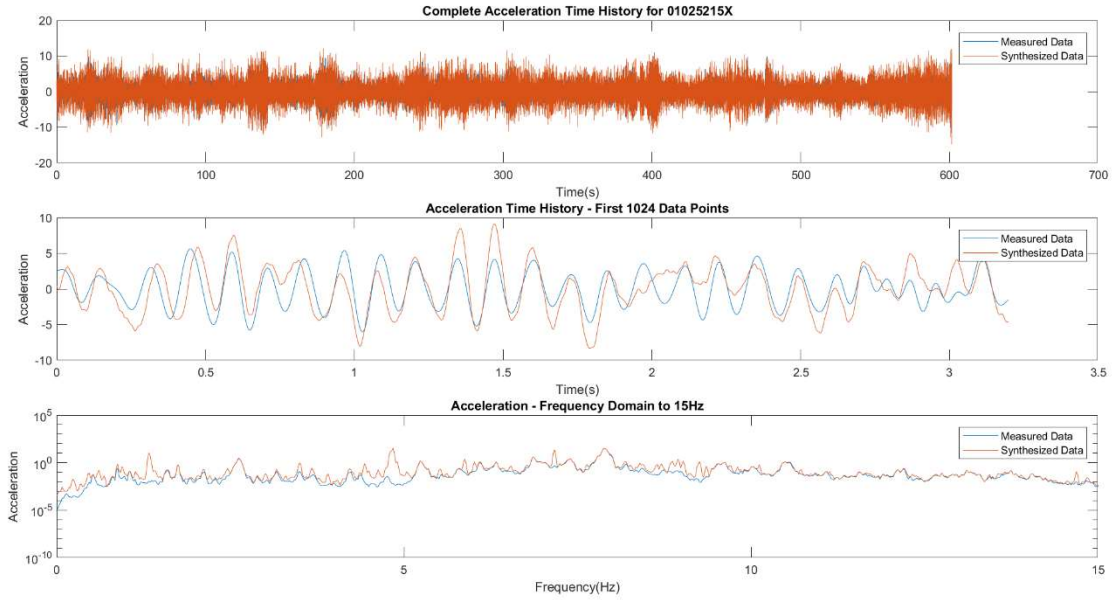

Figure 3: Simulated Acceleration (Blue Line) Compared to Reconstructed Acceleration (Orange Line) in the Vertical (X) Direction Below-JEL Corner A for the CT+MLP System in Motion at .9mph

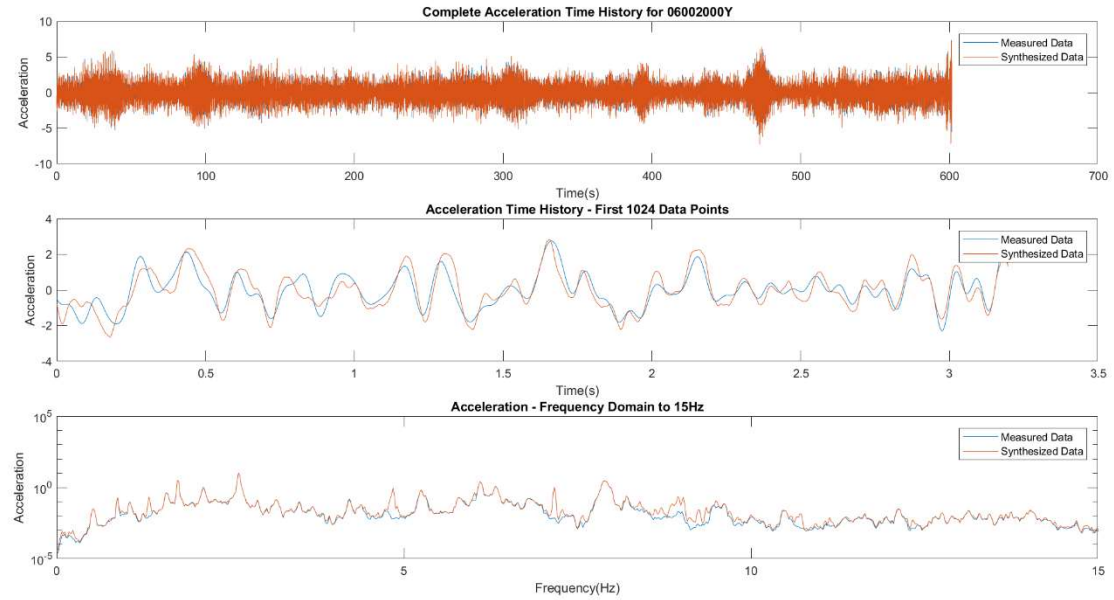

Figure 4: Simulated Acceleration (Blue Line) Compared to Reconstructed Acceleration (Orange Line) in the Lateral (Y) Direction Above the JEL at Corner A for the CT+MLP System in Motion at .9mph

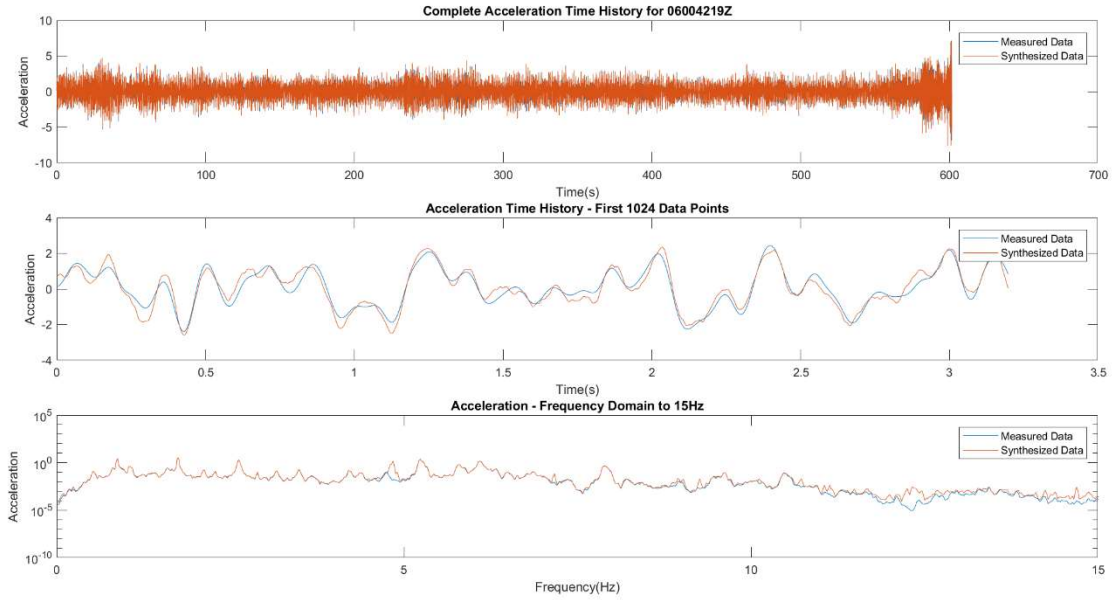

Figure 5: Simulated Acceleration (Blue Line) Compared to Reconstructed Acceleration (Orange Line) in the Fore/Aft (Z) Direction at Location 13 for the CT+MLP System in Motion at .9mph

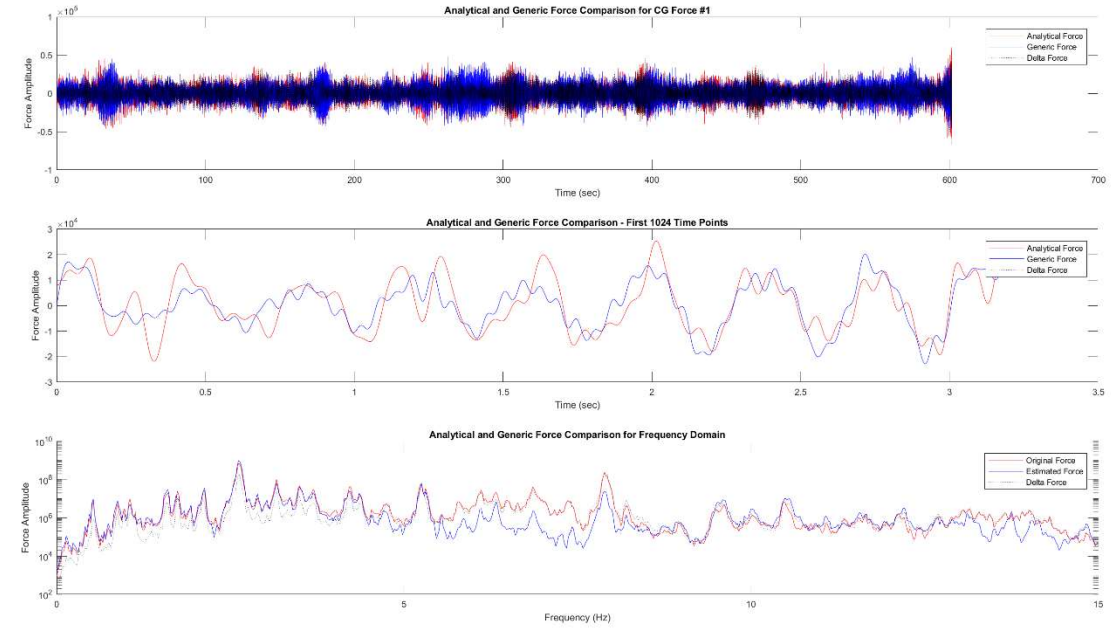

Figure 6: Reconstructed Analytical Force (Blue Line) Compared to Original Force (Red Line) in the Vertical (X) Direction at Corner A Below-JEL for the CT+MLP System in Motion at .9mph

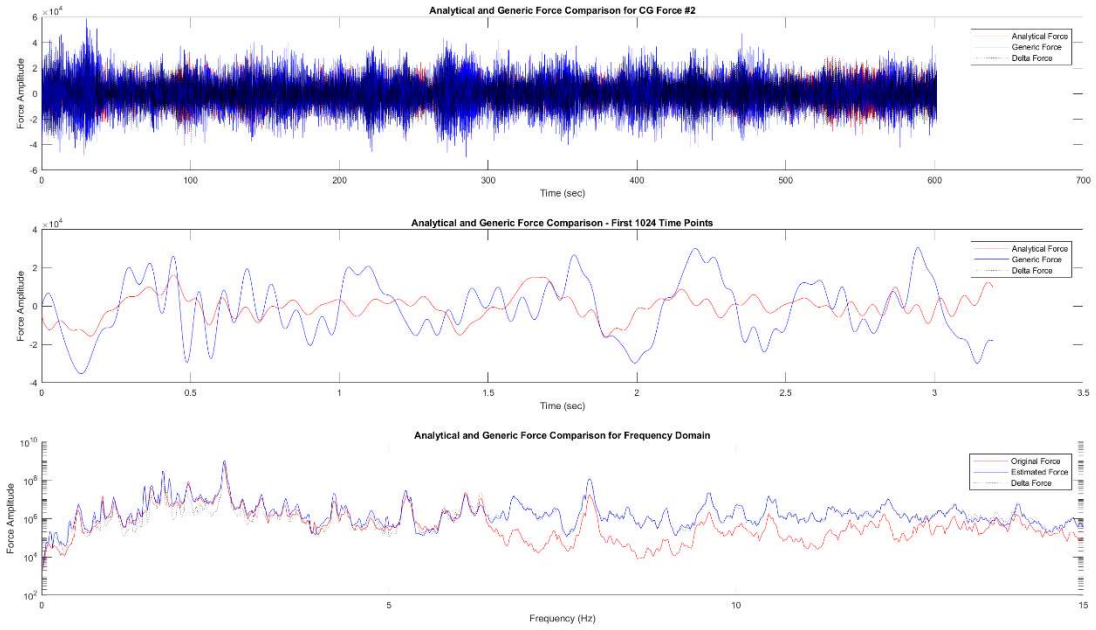

Figure 7: Reconstructed Analytical Force (Blue Line) Compared to Original Force (Red Line) in the Lateral (Y) Direction at Corner A Below-JEL for the CT+MLP System in Motion at .9mph

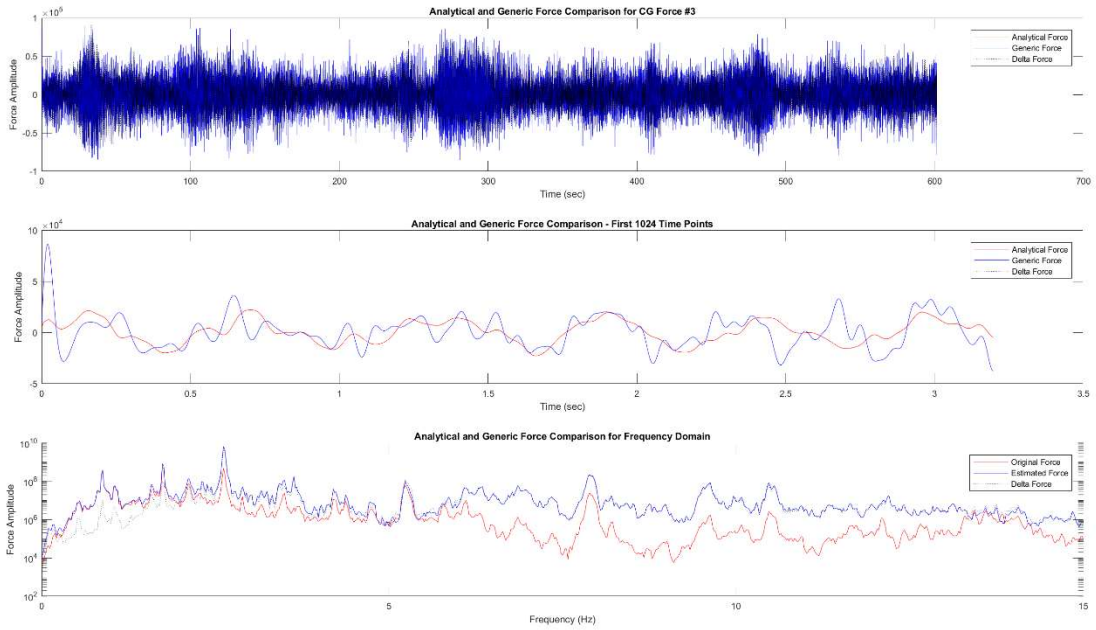

Figure 8: Reconstructed Analytical Force (Blue Line) Compared to Original Force (Red Line) in the Fore/Aft (Z) Direction at Corner A Below-JEL for the CT+MLP System in Motion at .9mph

Figure 9 provides a comparison of the frequency content between the frequency average of all the FRFs and a frequency average of the associated forcing function. The lower plot shows the autospectra of the averaged forcing function. Superimposed on this are vertical lines showing where the anticipated narrow-band harmonics are when traveling at .9mph. As described in previous references such as [7, 9, and 10], the harmonics expected while in motion at .9 mph include the following (in Hz): .5, .9, 1.1, 1.6, 1.8, 2.1, 2.6 (a strong combination harmonic), 3.2, 3.7, 4.2, 4.4, 4.8, 5.3 (a strong combination harmonic), 5.8, and 6.2 as well as weaker higher frequency continuations of this pattern. The peaks of the spectra line up with the anticipated frequencies, although there is a minor frequency dependent offset. This is likely due to numerical round-off errors in determining the expected harmonics or a minor numerical error in the defined speed of travel. There are also significant amplitude variations in the different harmonics.

The upper plot of Figure 9 provides a high-level comparison of the frequency content of the FRF. The average amplitude of all 12 x 63 = 756 FRFs is plotted with vertical lines denoting the expected analytical frequencies. A couple of lower frequency peaks are seen below the first flexible modes that are likely residual effects from the forcing function. The peaks near the first pair of flexible modes at 4.4Hz and the peak near the third flexible mode at 4.9Hz are the only significantly identifiable comparisons. However, these are showing some offsets that suggest a more refined data analysis is needed. Also, when compared to the lower plot, there are expected harmonics nearby that may be affecting the amplitudes. Another block of potential flexible peaks can be seen in the 6 to 7 Hz region.

A more detailed analysis utilized the full suite of 756 time domain Impulse Response Functions (IRFs) from the final FRF. The data analyzed were 8192 time steps in length. The quick-look assessment was made using the Eigensystem Realization Algorithm (ERA) with 1000 modes requested. The extracted modes were filtered for Consistent Mode Indicator (CMI) values greater than .1 and extracted damping values between 0% and 10%. Eleven modes were extracted and passed through these filters. Each of these extracted/filter modes were compared to each of the analytical modes of the system (as provided by the system FEM) below 12 Hz. The comparison results for the extracted mode at 5.92 Hz showed a reasonable correlation with an analytical mode (the 17th mode at 5.94Hz). Figure 10 shows the graphical comparison that captures these metrics to assess these extracted modes. The upper plot provides the Modal Assurance Criteria (MAC) comparison of the extracted modes to an individual analytical mode (the 17th analytical mode in this example) as red asterisks and the frequency of the analytical mode is denoted by the blue line. The successful extraction and comparison to an analytical of a mode is denoted by the blue line sitting on or near a red asterisk that has a high MAC value (MAC = .8 in Figure 10 for the 5.92 Hz mode). The middle plot contains the extracted frequencies versus damping (in % of critical). Ideally the extracted mode of interest would occur near the analytically imposed value for damping (1% is expected here). And the plot contains extracted frequency to the CMI, with the relevant value as high as possible. The 5.92 Hz mode is a member of a group of four modes with very close modal frequencies, all with significant vertical motion. It can be seen from Figure 2 that this model does have multiple sets of modes with very close frequencies (the regions of near vertical lines of points).

The CT+MLP system has been used in force estimation of rollout due as it is the least “dynamically active” configuration. This allowed the development of processes and models to support generic rollout forcing functions for use in analytical studies with untested systems (as in Reference [15]). However, this feature of the CT+MLP system suggests that many of the flexible modes of the system are hard to excite and creates a limited opportunity to address the third success criteria. The data assessed to date supports this conclusion. However, past work with more “dynamically active” systems has shown that flexible modes can be excited and even tuned in to harmonic resonances. Highly active systems using higher channel counts and additional speed content will provide richer comparisons and assessments for the third success metric. The 17th mode of the system, the CT chassis trampoline mode, is one of the most dynamically active and easy to excite modes of the CT+MLP system. Hence it is useful to target this mode as an example as it provides a metric by which to assess later data sets with dynamically sensitive elements. Figure 11 provides a bar chart representation of this mode with the response of the axial (X direction) sensor at the center of the CT chassis dominating.

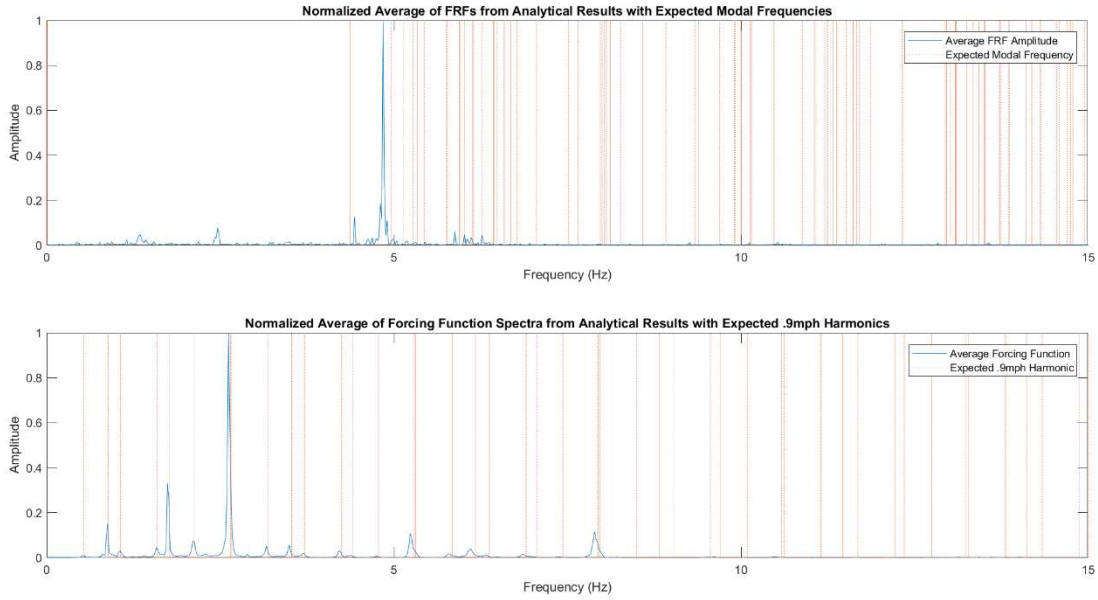

Figure 9: Frequency Comparison of the Average FRF and Forcing Functions as Estimated from Analytical Data to the Expected Harmonics and Analytical Modal Frequencies

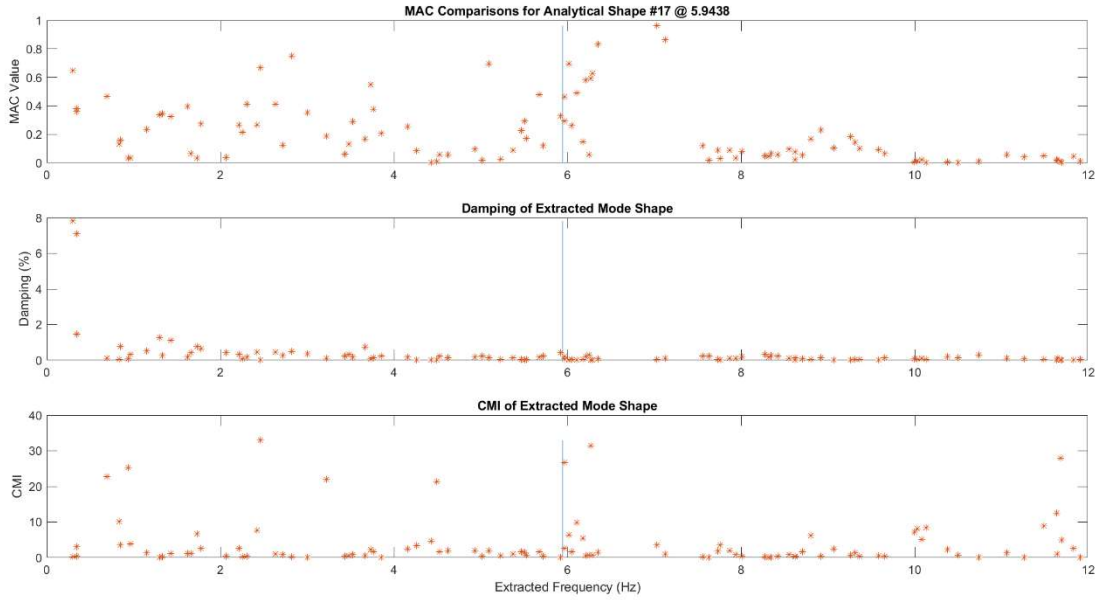

Figure 10: Modal Assurance Criteria (MAC), Damping, and Consistent Mode Indicator (CMI) Comparisons between the Extracted Modes and the Analytical 17th Mode at 5.94 Hz for the CT+MLP System

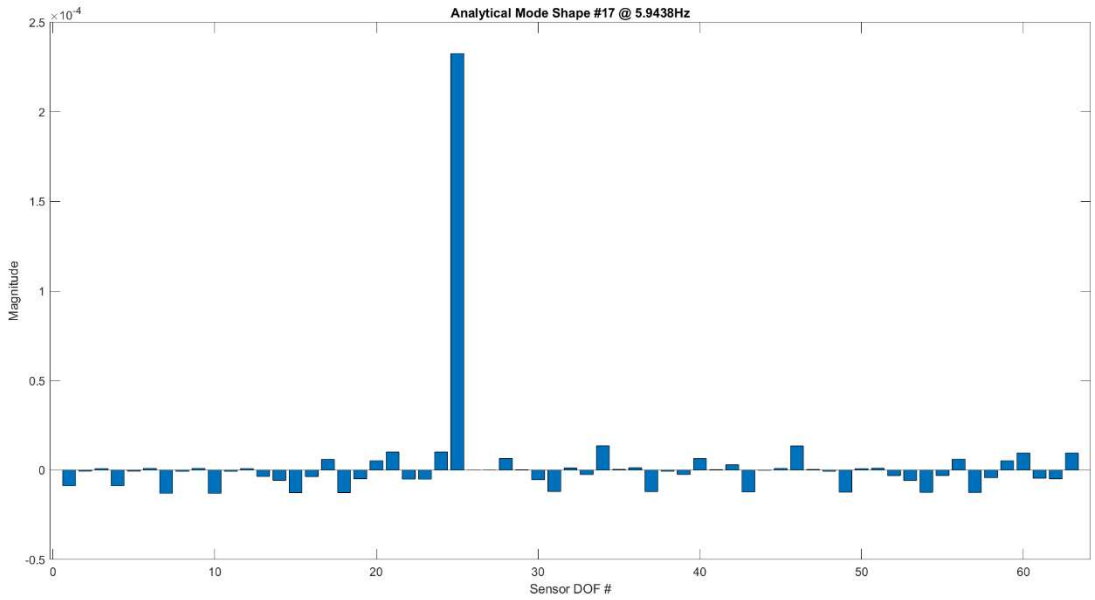

Figure 11: Bar Chart Representation of the Analytical 17th Mode at 5.94 Hz (CT Chassis Trampoline) for the CT+MLP System with Significant X Direction Motion at the Bottom Center of the Chassis

EXPERIMENTAL EXAMPLE

Data Set and Processing Description

A second example is provided using measured data from an actual rollout. Ten minutes of data taken at 320 samples/second was acquired with the CT+MLP system rolling at .9mph. Sixty-three accelerometer signals were acquired from the locations provided in Figures A2, A4, A6, and A7 as well as Tables A1 and A2. The above process was then applied to estimate the forcing functions and the system FRFs and IRFs. For this exercise, the measured output data was frequency filtered to 60Hz. A window size (*winsize*) of 16,384 was used with a *winskip0* increment of 8192 samples for FRF calculations. The *winskip1* time domain averaging increment was 256 samples. Step #9 and Step #12 were used for two forcing function iterations. The F_{CG} forces were not allowed to update with each iteration.

Results and Discussion

Figure 12 provides one of the 12 estimated forcing functions from this assessment. The harmonics expected during a roll at .9mph are seen in the estimated data. Figure 13 provides the corresponding accelerometer output at this location and direction. This location is a driving point location. Although there are some differences between the measured and reconstructed accelerations in the valleys and at the higher frequencies, the ability of the process to reproduce the measured data is clearly seen. Figure 14 provides the same information for the lateral (Y) direction at the CT/MLP interface above Truck A. The fit between reconstruction and measured data is very close. Figure 15 shows a fore/aft (Z) direction at the center of Side 3 of the upper MLP deck. This reconstruction is of the same quality as the other two directions. Overall, these reconstructions suggest that the process can be tuned to fit measured data with a reasonable chance of success. Note that the test-based Figures 13, 14, and 15 use the same output locations as the analysis-based Figures 3, 4, and 5.

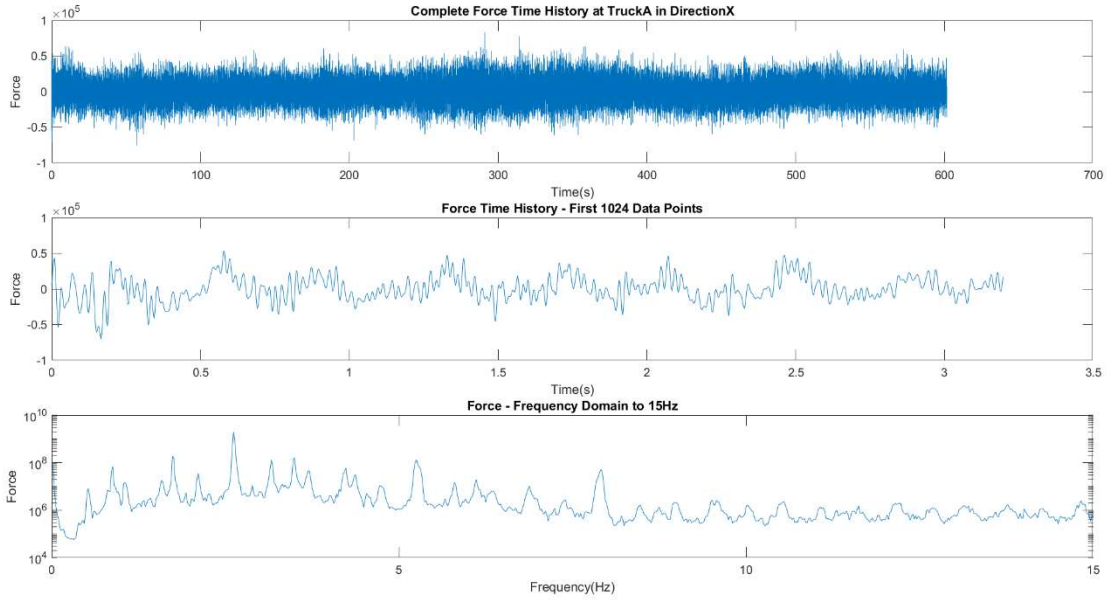

Figure 12: Force in the Vertical (X) Direction at Corner A Below-JEL as Estimated for the CT+MLP System in Motion at .9mph

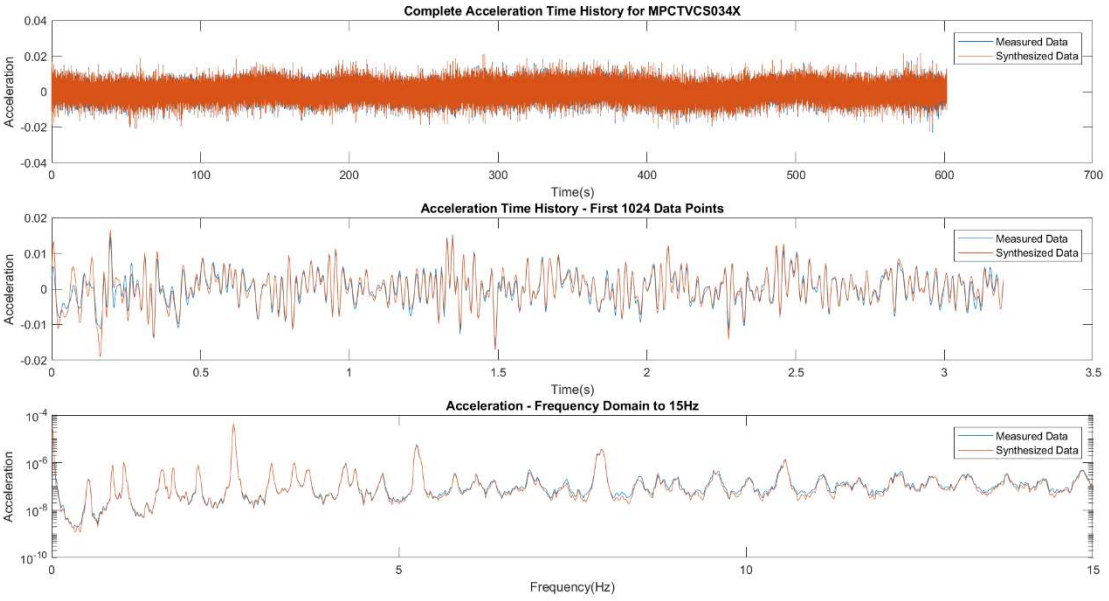

Figure 13: Synthesized Acceleration (Red Line) Compared to Measured Acceleration (Orange Line) for the Vertical (X) Direction at Corner A Below-JEL for the CT+MLP System in Motion at .9mph

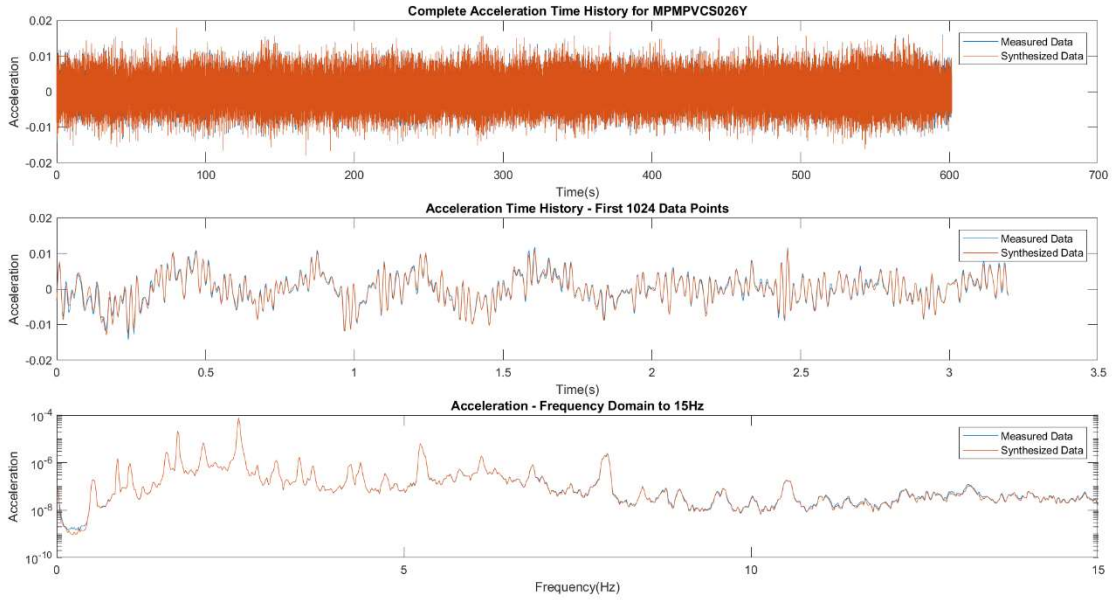

Figure 14: Synthesized Acceleration (Red Line) Compared to Measured Acceleration (Orange Line) for the Lateral (Y) Direction at the CT/MLP interface above Truck A for the CT+MLP System in Motion at .9mph

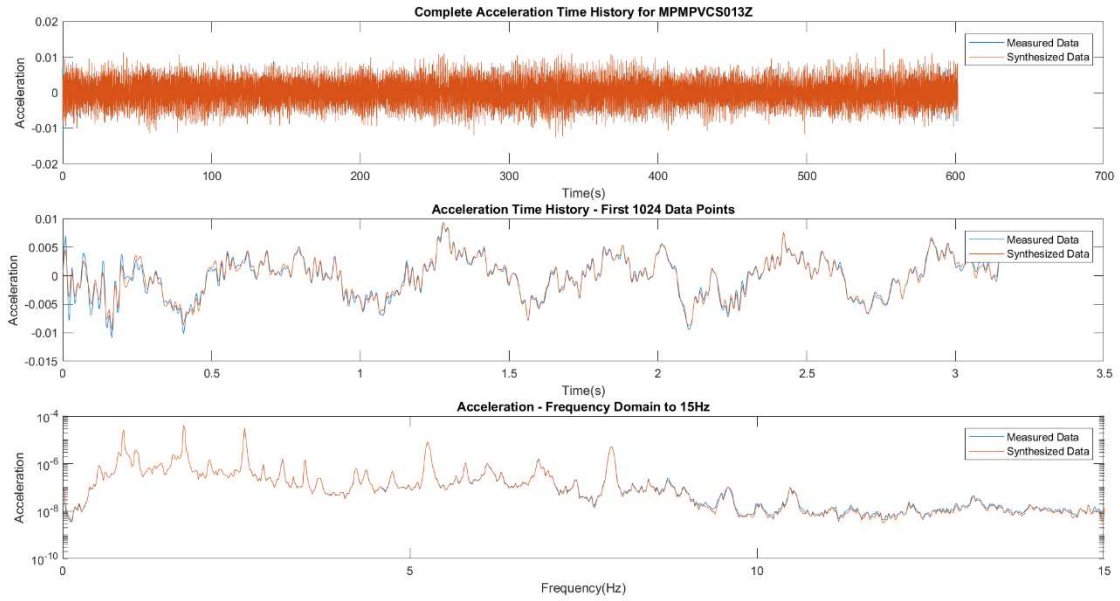

Figure 15: Synthesized Acceleration (Red Line) Compared to Measured Acceleration (Orange Line) for the Fore/Aft (Z) Direction at the Center of Side 3 on the Upper MLP Deck for the CT+MLP System in Motion at .9mph

Figure 16 provides one of the IRFs and one of the FRFs that resulted from the processing of this system. The specific functions chosen are the response in the Z direction at the center of Side 3 on the Upper MLP deck due to the input at Corner A Below-JEL. Note that these are the same output and input presented in Figures 12 and 15. The full IRF is in the top plot, the first 1024 time points of the IRF is in the second plot from the top. The amplitude of the FRF is in the third plot from the top, while the real and imaginary parts of the FRF are provided in the bottom plot. Note that the bottom two plots of Figure 16 do not show any significant frequency content in the measured data example until approximately 6 Hz. That suggests that the significant peaks in Figure 15 below 6 Hz are being driven largely from the forcing function harmonics without much dynamic amplification below the first dynamically active modes.

Figure 17 contains similar high-level frequency comparison data to Figure 9, except the forcing function and FRF estimates are developed from measured data as opposed to analytical FEM-generated data. The lower plot shows that the forcing function peaks line up with the expected harmonics as seen with the analytical data. The upper plots show that there are more potential dynamics in the measured system, especially in the 5 to 7 Hz and 11 to 13 Hz regions. However there are potential bleed-through frequencies from the forcing function at 2 Hz and below. The ability to more completely filter out harmonic forcing function frequencies from the FRF will require future work and additional data sets. Since the analytical model is not assumed to be perfectly correlated the measured data and the expected analytical modes may be off due to model mis-match. Data containing multiple speeds and a larger number of acceleration sensors would enhance the ability to sort forcing function harmonics from flexible modes. Since precursor work with earlier versions of these processes have been successful at extracting system modes, it is expected that successful identification of the system dynamic properties will be found in later studies (References [1, 9, 10, 15, and 16]).

Figure 18 shows that an extracted mode at 6 Hz has a MAC value of almost .8 when compared to analytical model #18. Figure 19 provides a bar chart representation of the 18th analytical mode, while Figure 20 provides a representation of the extracted mode with the closest MAC comparison (as seen in Figure 18). It can be seen that the mode at 6 Hz extracted from measured data appears to be a combination of the 17th analytical mode (Figure 11) and the 18th analytical mode (Figure 19). Note that these two modes have the same analytical modal frequency.

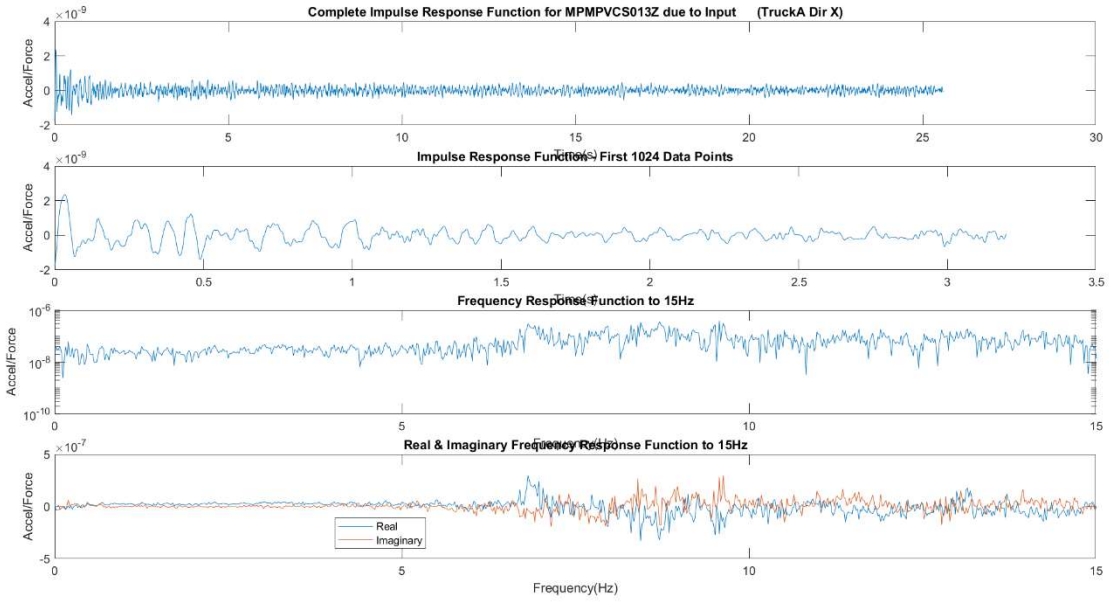

Figure 16: Estimated Impulse Response Function (IRF) and Frequency Response Function (FRF) between the Force Input at Corner A Below-JEL in the Vertical (X) Direction to the Fore/Aft (Z) Direction at the Center of Side 3 of the Upper MLP Deck for the CT+MLP System

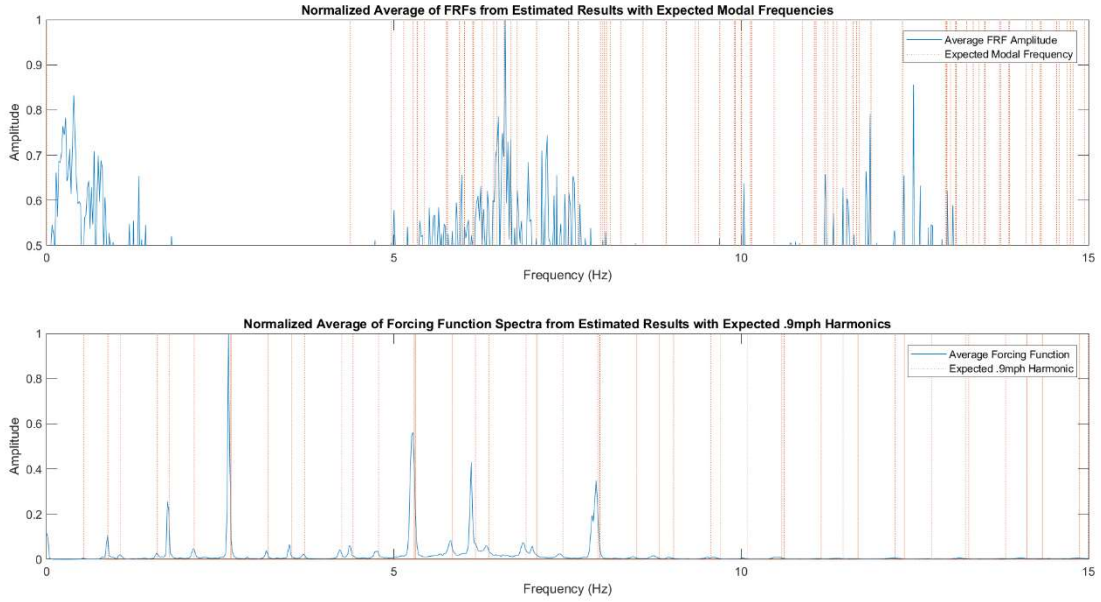

Figure 17: Frequency Comparison of the Average FRF and Forcing Functions as Estimated from Measured Data to the Expected Harmonics and Analytical Modal Frequencies

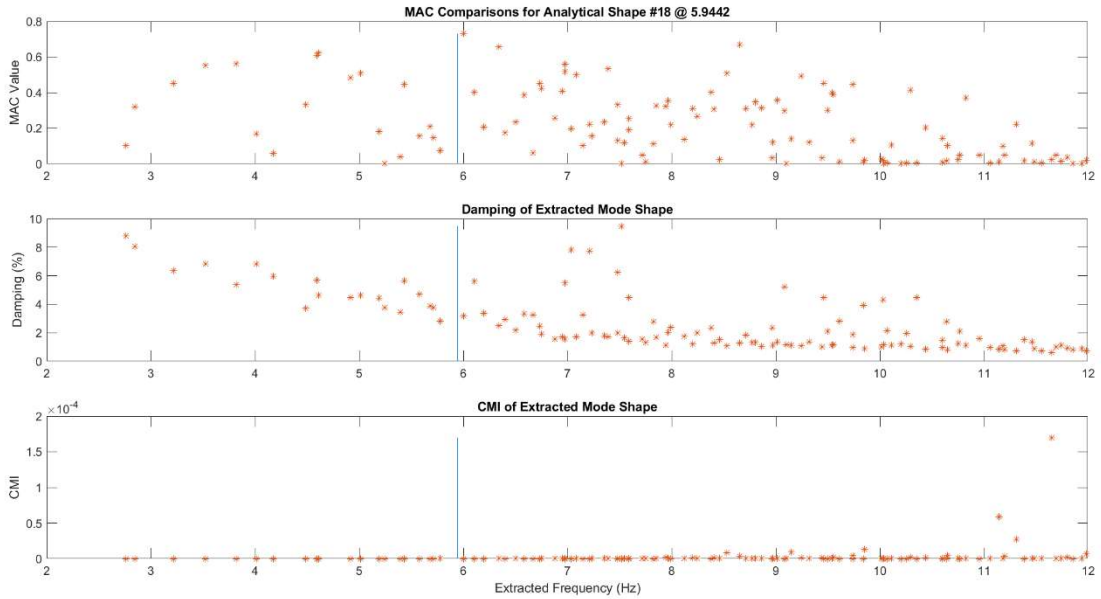

Figure 18: MAC, Damping, and CMI Comparisons between Extracted Modes and the Analytical 17th Mode at 5.94 Hz for the CT+MLP System

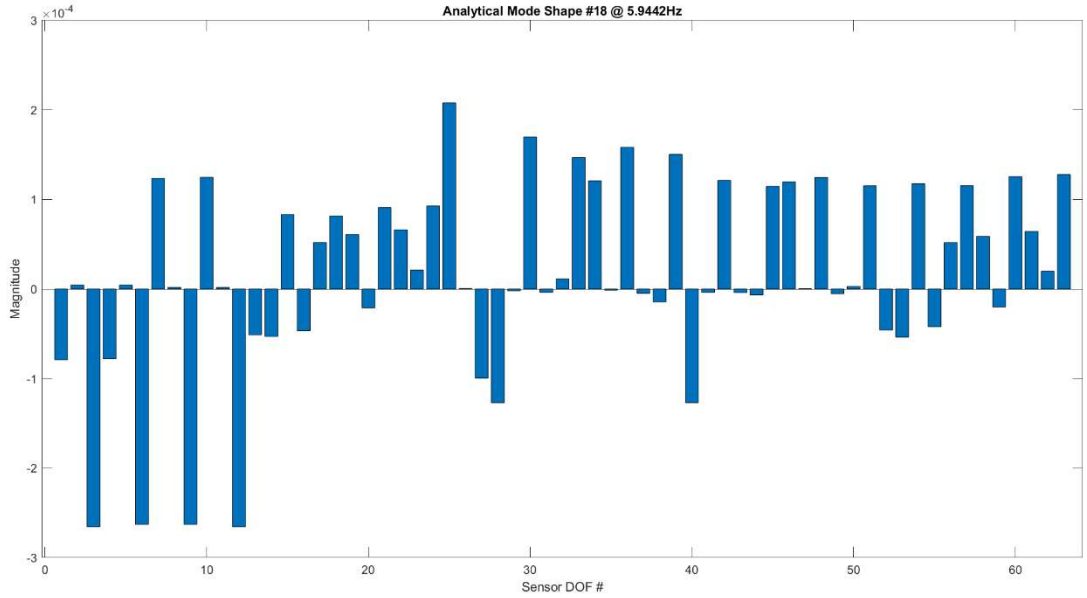

Figure 19: Bar Chart Representation of the Analytical 18th Mode at 5.94Hz (CT Truck Z Direction Out-Of-Phase with MLP) for the CT+MLP System (Repeated Mode with #17 Provided in Figure 18)

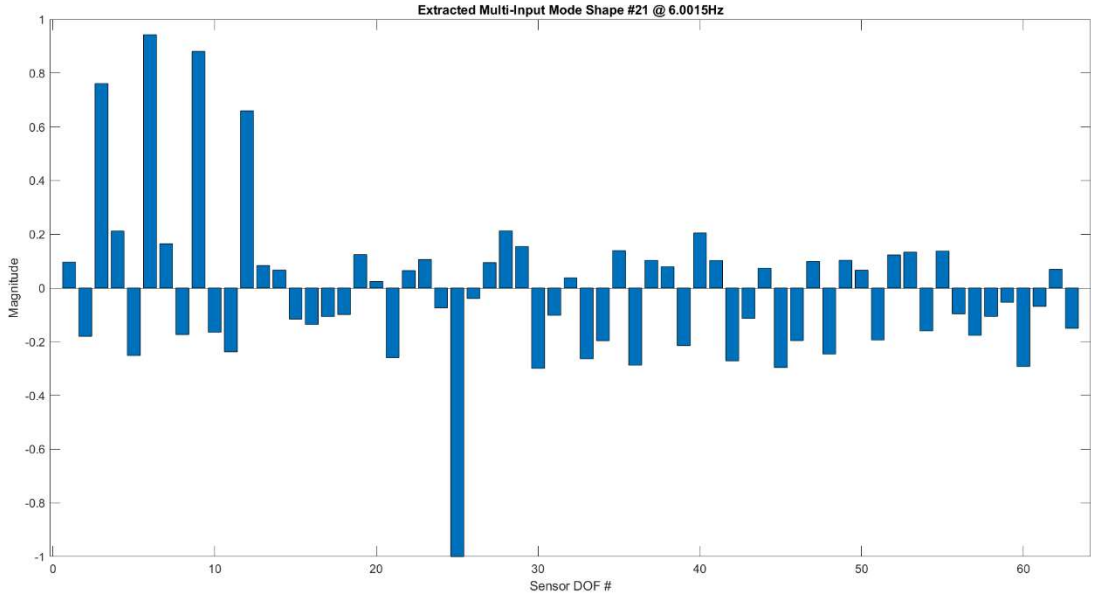

Figure 20: Bar Chart Representation of the Extracted Mode at 6 Hz (CT Truck Z Direction Combined with Chassis Trampoline) for the CT+MLP System (MAC .8 with Analytical Mode #18)

FUTURE WORK

The work reported in this paper represents an initial assessment into a larger more complete program. This work is intended to determine the applicability for larger scale diagnostic applications while at the same time focusing the efforts of smaller scale activities to develop process understanding. The detail-oriented side of these future efforts include potential tasks to more completely understand the foundational insight in these processes. These detail-oriented tasks include the following:

1. Laboratory scale articles where boundary conditions, forcing functions, and system dynamics are known;
2. Model sensitivity studies using the existing CT/MLP models, comparison of different FRF estimation schemes, and application of additional speed measurement sets;
3. Expanded analytical studies of full-scale systems with additional sensors, added dynamic receptivity, and more complex speeds/forcing functions; and
4. Application to existing rollout data sets with expanded sensor suites, system dynamics, and speed content.

Potential tasks to prepare for larger scale diagnostic applications include the following:

1. Apply current modal analysis tools to FRFs/IRFs resulting from these processes;
2. Application to simulated data of an operational system;
3. Application to rollout data with complex speed time histories, full sensor suites, realistic system dynamics, and operational constraints; and
4. Application to alternative systems in operational environments (such as launch vehicle in flight).

CONCLUSION

The process steps detailed herein are the result of efforts to implement tools to estimate a rollout FRF for the purpose of separating out the harmonics from the flexible body effects to allow estimation of the system's structural dynamic properties. Alternative paths are provided to assess the fidelity and robustness of different processing steps. This set of processing steps have been subjected to limited initial data sets to exercise, assess, modify as-needed, and verify the applicability to the systems that will be enhanced via operational testing. Systems that are difficult to test in controlled laboratory environments or subject to unusual boundary conditions and/or loading such as full launch stacks, spacecraft in-flight, or systems in transportation are targeted stakeholders. The results, processing updates, and assessments have not been finalized but do provide evidence that the processing tools can be successfully applied.

A process has been setup as a framework for the data analysis. Within this framework the following are unique contributions:

1. Expanding traditional CG centric force reconstruction techniques to expanded input locations and boundary conditions;
2. The use of CG force transformation matrix null space vectors as basis vectors to create full rank forces; and
3. Constrained least squares force updating to maintain targeted force updating.

Success criteria have been identified and initial but limited application data is available. The first success criteria (reproduction of the input data) appears to be met with the current processes as forcing function/FRF calculations can be fit to match the measured data with the full system data example covering this example. The second success criteria (proper estimation of forcing functions and transfer functions) has shown to have a positive potential based on a comparisons presented herein. A reasonable assessment of the third success criteria will need a more dynamically active data set as well as a more complete assessment of FRF calculation.

In summary, the processes developed herein hold promise to allow operational data to be used to derive structural dynamic parameters for multiple uses including but not limited to system identification, forcing function development, fatigue spectra generation, design assessment, and structural health monitoring, while expanding the reach of operational modal analysis.

ACKNOWLEDGEMENTS

The authors with to acknowledge Curt Larsen for his original insight to support this work. The team is also greatly indebted to Joel Sills for the continuing support and efforts to keep this work integrated into the larger scope of exploration initiatives within NASA. Multiple groups and individuals supporting the Space Launch System including structural dynamic, ground operations, and rollout analysis specifically have contributed significantly to this work, yet are too numerous to name here.

REFERENCES

[1] G.H. James, T.G. Carne, and J.P. Lauffer, "The Natural Excitation Technique (NExT) for Modal Parameter Extraction from Operating Structures," SEM *International Journal of Analytical and Experimental Modal Analysis*, Vol. 10, No. 4, October 1995.

[2] C. R. Farrar and G. H. James, "System Identification from Ambient Vibration Measurements on a Bridge," *Journal of Sound and Vibration*, Vol. 205, No. 1, 1997, pp. 1-18.

[3] R. Buehrle and K. Kappus, "Operating Deflection Shapes for the Space Shuttle Partial Stack Rollout", *Proceedings of the 23th International Modal Analysis Conference*, Orlando, FL, Jan. 31 – Feb. 3, 2005.

[4] G. H. James, "Testing Large Structures in the Field", *Proceedings of the 27th International Modal Analysis Conference*, Orlando, FL, February 9-12, 2009.

[5] T. G. Carne and G. H. James, "The Inception of OMA in the Modal Testing Technology for Wind Turbines", *Mechanical Systems and Signal Processing*, July 2010, pp. 1213-1226.

[6] G. James and others, "Extraction of Modal Parameters from Flight Data", *Proceedings of the 29th International Modal Analysis Conference*, Jacksonville, FL, January 31 – February 3, 2011.

[7] G. James, T. Carne, K. Elliott, and B. Wilson, "Estimation of the Space Shuttle Roll-Out Forcing Function", *Proceedings of the 23rd International Modal Analysis Conference*, Orlando, FL, January 31 – February 3, 2005.

[8] G. James, M. Kaouk, and T. Cao, "Progress in Operational Analysis of Launch Vehicles in Nonstationary Flight", *Proceedings of the 31st International Modal Analysis Conference*, Garden Grove, CA, February 11-14, 2013.

[9] G. James, J.-M. Tucker, G. Valle, R. Grady, J. Schliesing, J. Fahling, B. Emory and S. Armand, "Development of a Refined Space Vehicle Rollout Forcing Function," in *58th AIAA/ASCE/AHS/ASC Structures, Structural Dynamics, and Materials Conference*, AIAA SciTech Forum, Grapevine, TX, 2017.

[10] G. James, T. Carne, and B. Wilson., "Reconstruction of the Space Shuttle Roll-Out Forcing Function", *Proceedings of the 25th International Modal Analysis Conference*, Orlando, FL, February 19-23, 2007.

[11] M. Chamberlain and S. Hahn, "Reconstruction of Ares I-X Integrated Vehicle Rollout Loads", *Proceedings of the 52nd AIAA/ASME/ASCE/AHS/ASC Structures, Structural Dynamics, and Materials Conference*, Denver, CO, April 4-7, 2011.

[12] K. Elliott, G. James, R. Buehrle, and J. Richart, "Space Shuttle Transportation (Roll-Out) Loads Diagnostics", *Proceedings of the 23rd International Modal Analysis Conference*, Orlando, FL, January 31 – February 3, 2005.

[13] T. Carne, V. Bateman, and R. Mayes, "Force Reconstruction Using a Sum of Weighted Accelerations Technique", *Proceedings of the 10th International Modal Analysis Conference*, San Diego, CA, Feb. 3-7, 1992.

[14] M. Allen and T. Carne, "Comparison of Inverse Structural Filter (ISF) and Sum of Weighted Accelerations Technique (SWAT) Time Domain Force Identification Methods*", Proceedings of the 47th AIAA/ASME/ASCE/ AHS/ASC Structures, Structural Dynamics, and Materials Conference*, Newport, RI, May 1-4, 2006.

[15] J. Sills, G. James, R. Grady, G. Valle, J. Fahling, and E. Bruno, "Development of Generic Crawler/Transporter Rollout Forcing Functions for Coupled System Dynamic Analyses", ESD 20038, NASA Johnson Space Center, July 24, 2018.

[16] J. Sills, G. James, and E. Bruno, "Space Launch System (SLS) Dynamic Rollout Test (DRT) Preliminary Sensor Assessment", ESD 20048, NASA Johnson Space Center, July 24, 2019.

[17] J. L. Junkins, *An Introduction to Optimal Estimation of Dynamical Systems*, Sijthoff and Noordhoff, 1978.

[18] K. Nepolitano, "Using Singular Value Decomposition to Estimate Frequency Response Functions", *Proceedings of the 34th International Modal Analysis Conference*, Orlando FL, January 25-28, 2016.

APPENDIX A – HARDWARE AND DATA BACKGROUND

Crawler-Transporter (CT) Hardware

Rollout forces are generated as the CT imposes a series of harmonic excitations (sine and cosine-like waveforms) onto the entire system under transport. Previous work during rollout of the STS system found two primary families of harmonics, which are characterized by a speed-dependent harmonic and integer frequency super harmonics [7, 12]. This loading is inherent in the tracked vehicle design of the CT. Figure A1 shows one of the four *trucks* on the CT and one of the eight *tracks* on the CT. The *trucks* contain the drive trains. A *track* is the continuous collection of *shoes* that transfers the motive force from the CT to the ground. The *shoes* are the structural contact between the CT and the ground. The *rollers* carry the transported weight to the *shoes*. The spacing between two of the 57 *shoes* on each *track* and the spacing between two of the 11 *rollers* on each track define the two harmonic families of the forcing functions of interest. Note that vehicle response can significantly increase when one of these forcing function harmonics created by the *shoes* and *rollers* is at or near one of the resonant frequencies of the transported vehicle. Previous work found that these forcing functions do not act as pure harmonics. The load paths through the *trucks* and *rollers* of the CT change over time during roll based on (as-yet) undetermined factors. Although harmonic frequencies of the forcing function may stay relatively constant at constant speed, other parameter changes (such as harmonic amplitudes and phase) make the forcing function difficult to model analytically.

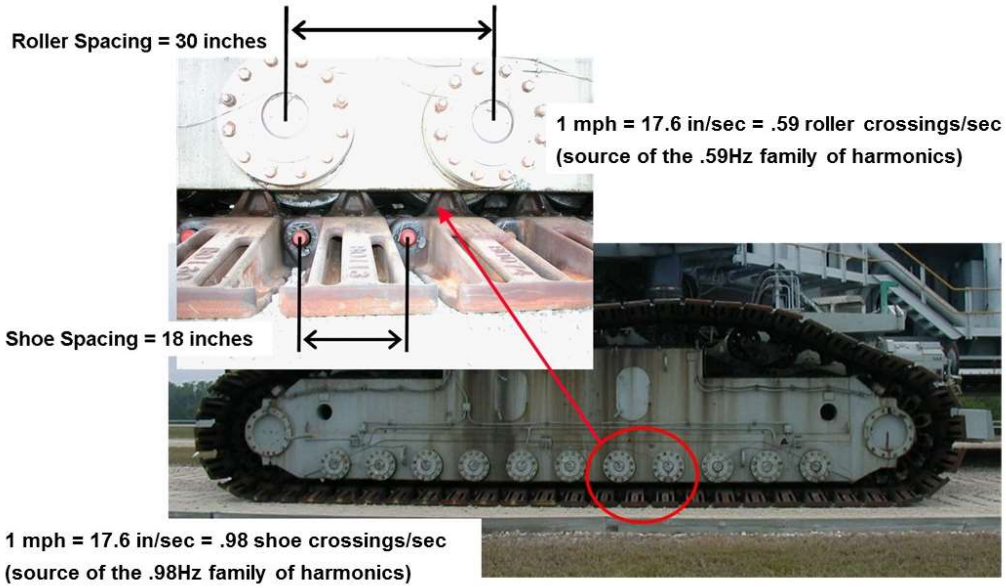

Figure A1: Crawler-Transporter (CT) Truck and Track with Critical Spacing Locations Identified

Each of the four *trucks* has a Jacking, Elevation, and Leveling (*JEL*) system and a *guide tube* system to properly support the CT *chassis* and the payload (launch platform and launch vehicle) as well as four electric *track* motors to provide motive force. The *guide tube* transfers all lateral loads from the CT *chassis*, the launch platform, and the launch vehicle into each of the four *trucks*. Figure A2 shows a schematic of a CT *truck* with the *tracks*, *track motors*, and *guide tube* marked.

All vertical forces generated to support the CT *chassis*, launch platform, and launch vehicle, are carried via the *JEL* systems. Each *truck* has four hydraulic cylinders that comprise the *JEL* system. The variability of the *JEL* system allows the CT to carry variable weight payloads, to handle uneven weight dispersions, to lift and lower the payload, and to level the payload when moving up or down the ramp at the pad. The CT *chassis* provides the structural framework to connect and control/steer all four *trucks* as well as interface to the payload. Also the *chassis* contains the diesel motors that drive the generators for motive and auxiliary power. The *chassis* contains the hydraulic systems for the *JEL* and steering functions. And finally all control interfaces to allow operation of the CT are housed in the *chassis*. Figure 4 shows a schematic and a photo showing the location and configuration of the *JEL* system on each *truck*, as well as the CT *chassis*. Note that one of the four payload support points is denoted in Figure A3. There is a pickup point for the payload at the center of each set of 4 JEL cylinders.

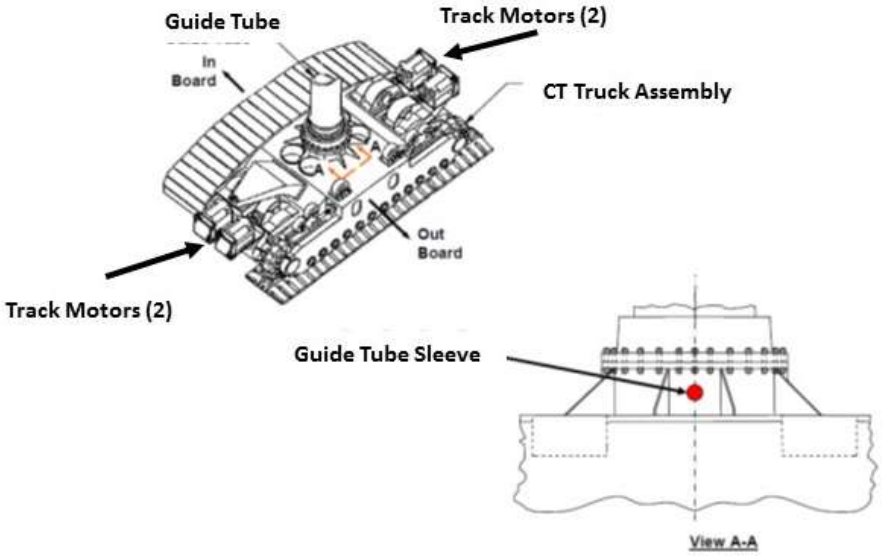

Figure A2: Crawler-Transporter (CT) Drive Motors and Guide Tube Systems Identified

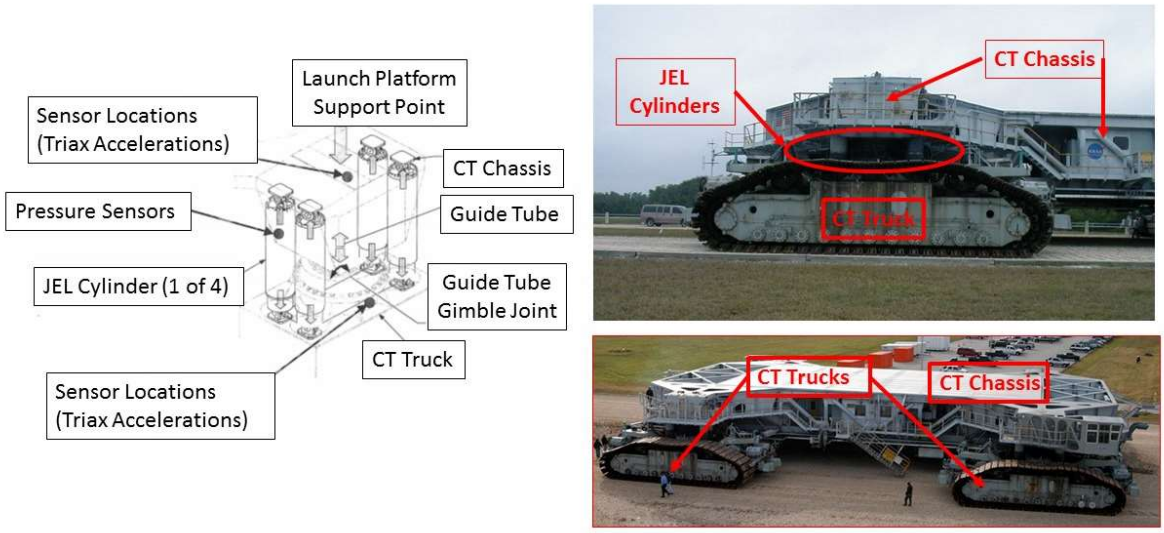

Figure A3: Crawler-Transporter (CT) Chassis and Jacking, Elevation, and Leveling (JEL) Systems Identified

Crawler-Transporter (CT) Sensor Suite

The CT has triaxial accelerometers mounted at 9 locations. Figure A4 shows the CT with Sides, Trucks (Corners), and lateral sensor locations denoted (on the upper surface). Table A1 provides more details on the locations of the sensor suite.

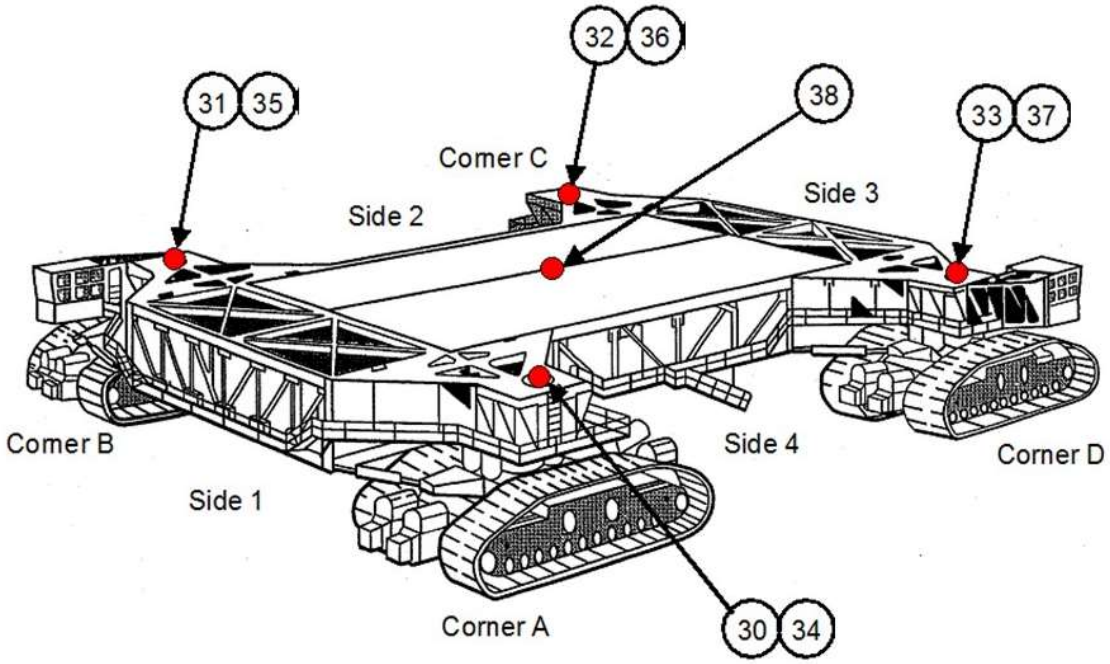

Figure A4: Crawler-Transporter (CT) with Standard Sensor Suite Denoted

Table A1: Crawler-Transporter (CT) Sensor Locations

#	Component	Vertical Location	Lateral Location	Channel Count
30	Truck A	Above JEL	Figure 5 as denoted	Triax
31	Truck B	Above JEL	Figure 5 as denoted	Triax
32	Truck C	Above JEL	Figure 5 as denoted	Triax
33	Truck D	Above JEL	Figure 5 as denoted	Triax
34	Truck A	Below JEL	Figure 3 Guide Tube Sleeve	Triax
35	Truck B	Below JEL	Figure 3 Guide Tube Sleeve	Triax
36	Truck C	Below JEL	Figure 3 Guide Tube Sleeve	Triax
37	Truck D	Below JEL	Figure 3 Guide Tube Sleeve	Triax
38	Chassis	Bottom Center	Chassis Bottom Below Figure 5 location	Triax

STS Mobile Launch Platform and Sensor Suite

The data in this paper will focus on an unloaded STS Mobile Launch Platform (MLP) carried by a CT. The MLPs were used to stack, transport, and launch the STS and Ares 1-X vehicles. Figure A5 shows an MLP on a CT system. The MLP weighs 8.2 million pounds without a vehicle. The CT weighs approximately one million pounds unloaded. The MLP/CT system represents a dynamically "simple" data set for a loaded CT. Since no vehicle is mounted on the MLP, there are no easily excited low frequency vehicle modes. The first major modes of this system are around 4.5 Hz. This configuration was operated for 10 minutes at five constant speeds (.5mph, .6mph, .7mph, .8mph, and .9mph) and at 0mph (stationary data). Only the .9mph data is used in the work reported herein. For the MLP, there were 12 triaxial sensor locations. Figure A6 shows the lateral locations of the sensors on Level B (the lower level). Figure A7 shows the lateral locations of the sensors on Level A (the upper level). Table A2 provides additional location information for the sensors.

Figure A5: Crawler-Transporter (CT) Moving a Space Shuttle Mobile Launch Platform (MLP)

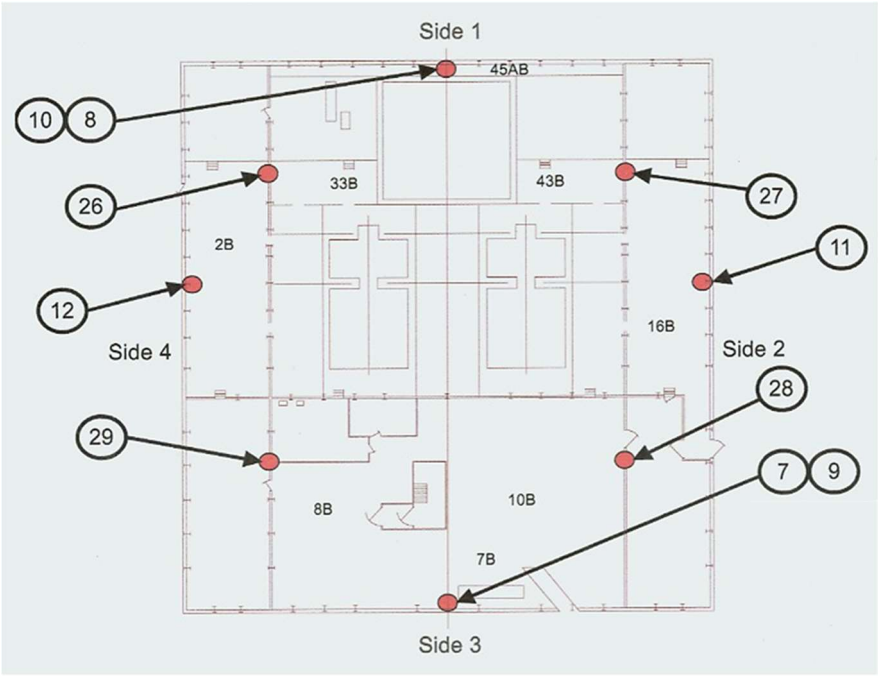

Figure A6: Mobile Launch Platform (MLP) Level B (Lower Level) with Sensor Locations Denoted

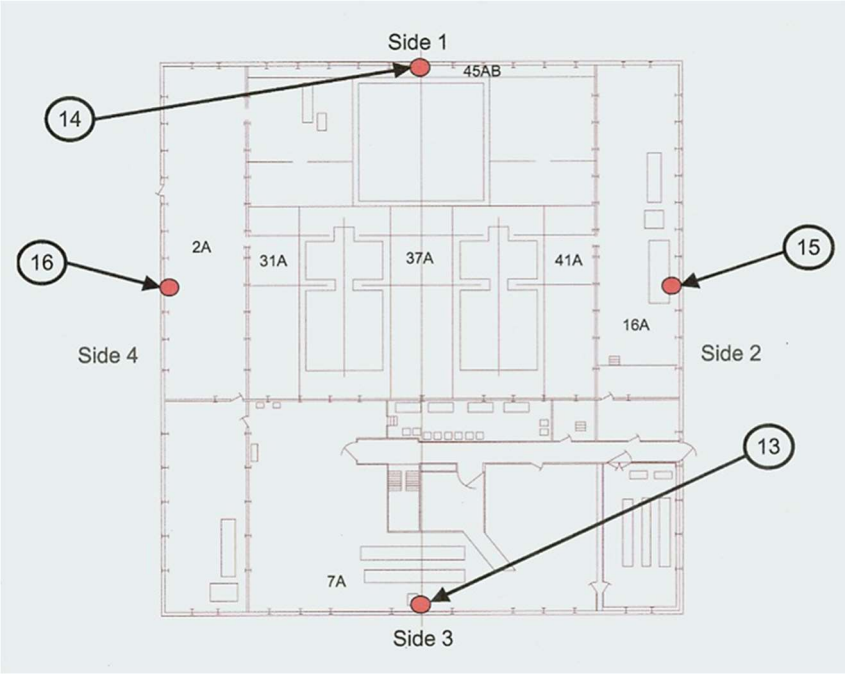

Figure A7: Mobile Launch Platform (MLP) Level A (Upper Level) with Sensor Locations Denoted

Table A2: Mobile Launch Platform (MLP) Sensor Locations

#	Component	Axial Location	Lateral Location	Channel Count
9	Level B	Lower Level	Side 3	Triax
10	Level B	Lower Level	Side 1	Triax
11	Level B	Lower Level	Side 2	Triax
12	Level B	Lower Level	Side 4	Triax
13	Level A	Upper Level	Side 3	Triax
14	Level A	Upper Level	Side 1	Triax
15	Level A	Upper Level	Side 2	Triax
16	Level A	Upper Level	Side 4	Triax
26	Pick-up Point	Bottom of MLP	Truck A	Triax
27	Pick-up Point	Bottom of MLP	Truck B	Triax
28	Pick-up Point	Bottom of MLP	Truck C	Triax
29	Pick-up Point	Bottom of MLP	Truck D	Triax